Università degli Studi di Roma "Tor Vergata"

Tesi di Laurea Magistrale in Fisica

Search for an Invisible Decaying Higgs Boson in Dilepton Events with the CDF detector at the Fermilab Tevatron Collider

Advisors
Prof. Giorgio Bellettini
Prof. Anna Di Ciaccio

Candidate
Cristiana Principato

Supervisor
Dr. Matteo Cremonesi

A. A. 2013/2014

Contents

0.1 Introduction

The Higgs boson plays a unique and important role in the Standard Model. It is the only scalar elementary particle in the theory. It is a boson, but it does not carry a force. The existence of the Higgs confirms our understanding of the mechanism by which particles have mass, and it is necessary to make the Standard Model re-normalizable.

The recent discovery of an Higgs-boson-like particle (named Higgs boson for simplicity in the following) at the LHC [[1], [2]], consistent with findings by the CDF and DØ collaborations at the Tevatron [[3]], completes our picture of the SM. However, the SM does not give answers to many fundamental questions, for example how to understand the value of the electroweak scale i.e. the value of the Higgs mass within the model itself. One therefore has to test the SM nature of this Higgs state, once its discovery is fully confirmed. As the measurements for more channels of the Higgs boson decay become available, a comprehensive picture of the properties of the Higgs state becomes possible. In this frame one must consider whether or not the Higgs sector is as simple as envisioned in the SM.

Since the properties of the standard model Higgs are precisely known, such measurements serve as a window to physics Beyond the Standard Model (BSM).

One such property is the Higgs decay width. In the SM, the width of the Higgs boson is calculated to be $\Gamma_H = 4$ MeV. Intrinsic detector resolution is on the order of a few GeV in the most well-measured channels. Therefore, direct limits are inherently weak, with $\Gamma_H < 1000\Gamma_H{}^{SM}$, leaving room for Physics Beyond the Standard Model (BSM). In particular, the Higgs decay width to invisible particles serves as a sensitive probe of BSM physics because the Standard Model background is small. The presence of massive, invisible BSM particles could significantly increase this width.

The invisible Higgs decay channel is also important in the search for additional Higgs bosons. While additional SM-like Higgs bosons have been excluded over a wide range of masses, those with exotic decay modes remain a possibility.

The new states could happen to not be detectable, resulting in missing transverse energy in our detector.

The most exploitable channel, at the Tevatron, is associated production with the Z boson, $q\bar{q} \to Z^* \to ZH$. In fact the presence of an on-shell Z provides two high p_T leptons in the final state, a clear signature for the trigger, together with other a significant amount of $\not{E}_T$ in our detector.

In this work, we perform a search at CDF for invisible Higgs decays in proton

anti-proton collision events produced at the Tevatron collider at $\sqrt{s} = 1.96$ TeV, corresponding to an integrated luminosity of $\approx 9.7 fb^{-1}$.

In Chapter 1 the Higgs mechanism in the Standard Model scenario is presented from a theoretical point of view. Chapter 2 is focused on the Higgs boson physics. The production and decay Higgs boson properties at the Tevatron collider are outlined, and the most viable channels for invisible decaying Higgs bosons are discussed. The possible scenarios for the invisible decays of Higgs boson are briefly reviewed, as well as the current status of searches for such scenarios, including existing global data fits. In Chapter 3 the CDF detector is described, as well as the online triggers selecting the lepton categories of interest. The identification and reconstruction performances for muons and electrons are also reported at the end of this chapter focusing on their role for the analysis.

In Chapter 4 the event selection and the cut-based analysis are described, focusing on the decay channel of the Z in ZH bosons which subsequently decay in 2 leptons and missing transverse energy. In Chapter 5 the irreducible and reducible backgrounds to this decay channel are presented. The irreducible background has been studied outside the Z boson mass window: its normalization and kinematic properties have been checked. Control regions have been defined in order to check the reducible background distribution and to determine its normalization. In Chapter 6 the results of the analysis, obtained by means of a Confidence Level (CL) calculation in the Bayesian approach are presented.

Chapter 1

Theoretical background
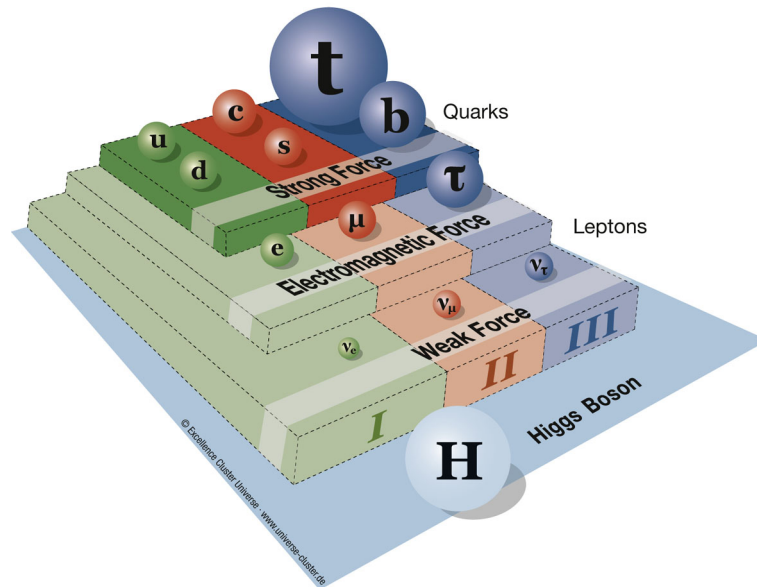
Figure 1.1: The 'standard model' of elementary particle physics: the building blocks of matter and the forces that operate between them

1.1 Particles and Fields

The SM is a quantum field theory in which particles are treated as local quantum fields interacting via the exchange of force mediators (each type of force has its own mediators), that are introduced in order to conserve local symmetries i.e. the theory has to be *gauge invariant* under local transformations [4].

4

The SM is based on the gauge symmetry group $SU(3) \otimes SU(2) \otimes SU(1)$: $SU(3)$ describes the QCD (Quantum-Chromo-Dynamics) theory of strong interactions, $SU(2)$ describes the weak theory and $SU(1)$ the QED (Quantum-Electro-Dynamics) theory of electromagnetism.

As summarized in table 1.1, elementary particles are divided in two fundamental groups by their spin: leptons and quarks, with half-integer spin, and bosons, with integer spin. Quarks and leptons follow the Fermi-Dirac statistics and are called *fermions*, while *bosons* follow the Bose-Einstein statistics.

	Name	Symbol	Spin ($\hbar$)	Charge (e)	Mass (MeV/c^2)
	e neutrino	ν_e	1/2	0	$< 2 \cdot 10^{-6}$
	electron	e	1/2	-1	$0.510998910 \pm 0.000000013$
Leptons	μ neutrino	ν_μ	1/2	0	< 0.19
	muon	μ	1/2	-1	$105.6583668 \pm 0.0000038$
	τ neutrino	ν_τ	1/2	0	< 18.2
	tau	τ	1/2	-1	$1.77 \pm^{0.16}_{0.16}$
	up	u	1/2	2/3	$2.49 \pm^{0.81}_{0.79}$
	down	d	1/2	-1/3	$5.5 \pm^{0.75}_{0.95}$
Quarks	charm	c	1/2	2/3	$(1.27 \pm^{0.07}_{0.09}) \cdot 10^3$
	strange	s	1/2	-1/3	$101 \pm^{29}_{31}$
	beauty	b	1/2	2/3	$(4.19 \pm^{0.18}_{0.06}) \cdot 10^3$
	top	t	1/2	-1/3	$(174.34 \pm^{0.64}_{0.64}) \cdot 10^3$
	photon	γ	1	0	0
Gauge Bosons	W boson	$W^\pm$	1	± 1	$(80.399 \pm 0.023) \cdot 10^3$
	Z boson	Z^0	1	0	$(91.1876 \pm 0.0021) \cdot 10^3$
	gluon	g	1	0	0

Table 1.1: Elementary particles in the SM and their properties (from [7]).

1.1.1 Fermions

The matter, as we know so far, is built up by fermions that are divided in two classes: leptons and quarks. For each fermion there is a corresponding anti-particle with the same mass and opposite quantum numbers. Each class can be ordered in three generations, also called *families* (see table 1.1). Only first generation particles can form stable matter, while second and third generations fermions are created by high-energy process and subsequently decay into first generation states.

Quarks exist in six different types, called *flavors*, as shown in table 1.1, with a fractional electric charge of 2/3 and -1/3. They interact through EM, weak and strong interaction. Quarks are bound by strong interactions into physical

states, called hadrons, of $q\bar{q}$ pairs (mesons) or three quarks (baryons). Pauli's principle prohibits fermions to occupy the same quantum state. As two u or d quarks combine stably into three-quark baryons, they must carry a new "color" quantum number, which can take three values named *color* flavor and results in three different types: red, yellow, blue. Bound states of quarks are color-neutral. Gluons, the strong force mediators, carry the color number itself, hence are self-coupled. This causes an increase of the force strength with the distance, so that quarks are tightly forced to be bound in hadrons (*confinement*) and they cannot be observed free.

Leptons interact via weak force and, if they carry electric charge, also via EM. They carry a *leptonic* number that characterizes each family. Neutrinos were originally assumed to be massless while several measurement showed that their mass is tiny but not zero (see table 1.1). [[5, 6]]. So far, no direct measurement of a ν mass exists [7].

1.1.2   Bosons and interactions

Interactions between particles in SM are mediated by spin 1 bosons: Photons (γ) mediate electromagnetic interaction, $W^{\pm}$ and Z^0 mediate weak interaction and color-carrying gluons (g) mediate strong interactions. Those particles are needed in the SM in order to maintain local invariance of the Lagrangian density function of the physical system. In fact, local phase transformations of the free Lagrangian density impose to introduce gauge fields (i.e. the gauge bosons) to preserve local gauge invariance. The invariance can be seen as a symmetry of the function and, according to Noether's theorem, when a symmetry is introduced in the system a conserved current verifying continuity equation is induced:

$$\partial_{\mu}J^{\mu} = 0 \tag{1.1}$$

Since the conservation of a current is associated with conservation of a charge (the time-component J^0 of 4-vector J^{μ} integrated over the space), it means that each interaction force has to conserve a quantum number: the electric charge Q in EM, the weak isospin charge I_3^W (and the associated weak hypercharge $Y = Q/e - I_3^W$) in weak interaction and color charge C_q in strong interaction [8]. Coupling with those charges, the gauge fields generates the interactions with strengths characterized by coupling constants with approximate relative magnitudes:

$$\alpha_{strong} : \alpha_{em} : \alpha_{weak} \approx \frac{1}{10} : \frac{1}{100} : \frac{1}{10000} \tag{1.2}$$

Typical lifetimes of processes belonging to those interactions are (in seconds):

$$\tau_{\text{strong}} \approx 10^{-23}, \quad \tau_{\text{em}} \approx 10^{-20} - 10^{-16}, \quad \tau_{\text{weak}} \approx 10^{-12} \tag{1.3}$$

Quantum Electrodynamics

The quantum field theory of electromagnetism is the quantum electrodynamics (QED). The Lagrangian density function in QED for a free-fermion is:

$$\mathscr{L}_0 = \bar{\psi}(x)(i\gamma^{\mu}\partial_{\mu} - m)\psi(x) \tag{1.4}$$

where ψ is the Dirac field of mass m. Although 1.4 is already invariant for *global* U(1) transformation $\psi \to e^{-iqf}\psi$, it is not invariant under *local* U(1) transformation (i.e. with a space-time dependent differentiable function f(x)):

$$\psi \to e^{-iqf(x)}\psi \tag{1.5}$$

Through the minimal substitution of the derivative with covariant derivative:

$$\partial_{\mu} \to D_{\mu} \equiv (\partial_{\mu} + iqA_{\mu}(x)) \tag{1.6}$$

where A_{μ} is the real electromagnetic field transforming as

$$A_{\mu} \to A_{\mu} - \frac{1}{q}\partial_{\mu}f(x) \tag{1.7}$$

the Lagrangian becomes invariant in the final form

$$\mathscr{L}_{QED} = \mathscr{L}_0 - q\bar{\psi}(x)\gamma^{\mu}\psi(x)A_{\mu}(x) - \frac{1}{4}F_{\mu\nu}F^{\mu\nu} \tag{1.8}$$

The second term in 1.8 represents the interaction between charged particles through the gauge field A_{μ}, i.e. the exchange of a photon. Local invariance also requires photon to be massless (otherwise, a term as $\frac{1}{2}mA_{\mu}A^{\mu}$ would emerge from the calculation), as experimentally verified. Finally, the masslessness of the photon also implies that electromagnetic interaction has infinite range.

Weak interaction

The first theory for weak processes was proposed by E. Fermi in 1934 [9]. In order to explain β-decay $n \to pe^{-}\bar{\nu}_e$, he introduced a current-current amplitude of the form:

$$\mathscr{M} = G_F(\bar{u}_p\gamma^\mu u_n)(\bar{u}_e\gamma_\mu u_{\nu_e}) \tag{1.9}$$

with the Fermi coupling constant $G_F/(\hbar c)^3 = 1.166 \cdot 10^{-5}$ GeV^{-2}. In 1957 C. S. Wu's experiment showed parity violation of ^{60}Co decay in ^{60}Ni that was not explained by Fermi's theory, therefore a new form of interaction was suggested by replacing γ^μ in Eq. 1.9 with $\gamma^\mu(1-\gamma^5)$. This is the so-called V-A structure of weak interactions that couples differently with left-handed and right-handed components of the spinors $\psi = \psi_L + \psi_R$ (i.e. the fermions). In high energy approximation[1], leptonic currents involve only left-handed lepton fields. Limited to the case of leptonic interactions (i.e. for e, μ, τ and the corresponding neutrinos), for any Dirac spinor $\psi(x)$ we can define the weak *isospin* doublet:

$$\Psi_l^L(x) \equiv \begin{pmatrix} \psi_{\nu_l}^L(x) \\ \psi_l^L(x) \end{pmatrix} \tag{1.10}$$

with

$$\psi_{l,\nu_l}^L(x) = \frac{1}{2}(1-\gamma_5)\psi_{l,\nu_l}(x) \tag{1.11}$$

The formulation of weak interaction as gauge theory relies on the invariance under $SU(2)$ local phase transformations:

$$\Psi_l^L(x) \rightarrow \Psi_l^L(x)e^{ig\alpha_j(x)\tau_j/2}, \qquad \bar{\Psi}_l^L(x) \rightarrow \bar{\Psi}_l^L(x)e^{-ig\alpha_j(x)\tau_j/2} \tag{1.12}$$

where g is the weak coupling constant, τ_j are Pauli spin matrices and $\alpha_j(x)$ are three arbitrary real differentiable functions of x. As it can be shown, we can obtain from this invariance three conserved weak currents:

$$J_j^\alpha(x) = \frac{1}{2}\bar{\Psi}_l^L(x)\gamma^\alpha\tau_j\Psi_l^L(x), \quad j = 1,2,3 \tag{1.13}$$

and finally the corresponding conserved charges, called *weak isospin charges*:

$$I_j^W = \int d^3x J_j^0(x), \quad j = 1,2,3 \tag{1.14}$$

The third current J_3^α is called *neutral* current, cause it couples also to electrically neutral leptons (i.e. neutrinos). As said above, we can define the *weak hypercharge* from the electric and weak charge:

$$\frac{Y}{2} = Q/e - I_3^W \tag{1.15}$$

---

[1]this weak theory is gauge-invariant only if leptons and bosons are considered massless. For high energy approximation we refer to E≫m.

so that left-handed ν_l has $I_3^W = \frac{1}{2}, Y = -1$ and the left-handed charged lepton has $I_3^W = -\frac{1}{2}, Y = -1$.

Flavor mixing: CKM matrix

Leptons form $SU(2)$ doublets under the weak interaction:

$$\begin{pmatrix} \nu_e \\ e \end{pmatrix}, \quad \begin{pmatrix} \nu_\mu \\ \mu \end{pmatrix}, \quad \begin{pmatrix} \nu_\tau \\ \tau \end{pmatrix} \tag{1.16}$$

For quarks, the experimentally verified flavor change via W boson exchange must be taken into account, so that hadronic coupling is possible using the CKM rotation on quarks d, s, b. In this case, the flavor states are different from the mass states:

$$\begin{pmatrix} u \\ d' \end{pmatrix}, \quad \begin{pmatrix} c \\ s' \end{pmatrix}, \quad \begin{pmatrix} t \\ b' \end{pmatrix} \tag{1.17}$$

where the Cabibbo-Kobayashi-Maskawa (CKM) matrix (an unitary 3X3 matrix) operates on mass states d, s, b:

$$\begin{pmatrix} d' \\ s' \\ b' \end{pmatrix} = \begin{pmatrix} V_{ud} & V_{us} & V_{ub} \\ V_{cd} & V_{cs} & V_{cb} \\ V_{td} & V_{ts} & V_{tb} \end{pmatrix} \begin{pmatrix} d \\ s \\ b \end{pmatrix} \tag{1.18}$$

Electro-Weak Unification

In 1961, Glashow [10] proposed an unified gauge theory for QED and weak interactions, based on $SU(2) \otimes U(1)$ group symmetry. Similar to QED, even the weak lagrangian density can be made invariant under local gauge transformations (Eq.1.12) through replacement of the derivative and the introduction of gauge fields. If we make both replacements valid for U(1) and SU(2) at same time:

$$\partial^\mu \rightarrow D^\mu = (\partial^\mu + ig\tau_j W_j^\mu(x)/2 - ig'B^\mu(x)/2) \tag{1.19}$$

where W^μ is the real vector gauge field for weak interactions (according to SU(2) symmetry) and B^μ is the real gauge field for QED (according to U(1)), we obtain the invariant leptonic electro-weak Lagrangian density in the form $\mathcal{L}^L = \mathcal{L}_0 + \mathcal{L}_I$, where

$$\mathcal{L}_I = \mathcal{L}_{CC} + \mathcal{L}_{NC} \tag{1.20}$$

CC and NC indicatating respectevely the charged and neutral currents. It is usually used a linear combination of $W_{1\mu}, W_{2\mu}$ for weak charged current while we write photon and Z^0 boson as linear combinations of B^μ and W_3^μ

$$W_\mu^{(\dagger)} = \frac{1}{\sqrt{2}}(W_{1\mu} \mp W_{2\mu}) \tag{1.21}$$

$$A_\mu = B_\mu \cos\theta_W + W_\mu^3 \sin\theta_W, \quad Z_\mu = -B_\mu \sin\theta_W + W_\mu^3 \sin\theta_W \tag{1.22}$$

$$g \sin\theta_W = g' \cos\theta_W = e \tag{1.23}$$

where θ_W is the Weinberg angle with a measured value of $\sin^2\theta_W = 0.2312 \pm 0.0006$ [7].

As we can see, from previuos formula it is straightforward to interpret the quanta of gauge fields as the EM and weak force mediators $\gamma, W^\pm, Z^0$.

So far, we have considered the fields as massless, as in Glashow's first theory, because of the gauge symmetry of the system. The Higgs mechanism was introduced to solve this problem adding the mass term for lepton and boson field, preserving at the same time gauge invariance.

1.1.3 Higgs mechanism: spontaneous symmetry breaking

The Higgs mechanism was proposed at the beginning of the '60s by several authors (Higgs, Englert, Guralnik et al.) [11, 12, 13] and has been fully incorporated into the SM by Weinberg and Salam [14, 15]. It relies on the idea to have a Lagrangian density invariant under a symmetry group of transformations that produces degenerate asymmetric states. By arbitrarily selecting one of one of these states we have a *spontaneous symmetry breaking*. The core of the mechanism is to find a non-unique ground state (i.e. the *vacuum*) that implies a non-vanishing quantity in the system. This quantity will be assumed as the vacuum expectation value of quantized field.

In its simplest configuration the Higgs mechanism can be shown in a scalar Lagrangian density:

$$\mathscr{L}(x) = (D^\mu \varphi(x))^*(D_\mu \varphi(x)) - \mu^2 \varphi^*(x)\varphi(x) - \lambda(\varphi^*(x)\varphi(x))^2 - \frac{1}{4}F_{\mu\nu}(x)F^{\mu\nu}(x) \tag{1.24}$$

where D^μ is the covariant derivative 1.6 so that $\mathcal{L}$ is invariant under U(1) gauge transformations 1.5, λ and μ^2 are real parameters and $\varphi(x)$ is a complex scalar field that interacts with the A_μ gauge field defined as usual by $F_{\mu\nu} = \partial_\nu A_\mu - \partial_\mu A_\nu$.
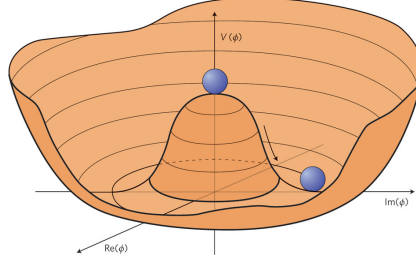
Figure 1.2: Symmetry breaking for a complex scalar field $\phi(x) = 1/\sqrt{2}[\phi_1(x) + i\phi_2(x)]$ choosing $\mu^2 > 0$ in $\mathscr{V}(\phi)$

The potential part of the field $\mathscr{V}(\phi) = \mu^2 \varphi^*(x)\varphi(x) + \lambda(\varphi^*(x)\varphi(x))^2$ depends on λ, μ^2. If we take $\lambda > 0$, two situations occour for the bounded potential: for $\mu^2 > 0$ $\mathscr{V}(\phi)$ has an absolute miminum at $\phi(x) = 0$, while for $\mu^2 < 0$ $\mathscr{V}(\phi)$ possesses a local minimum at $\phi(x) = 0$ and a whole circle of absolute minima, leading to a set of degenerate states i.e. different *vacuum states* (see 1.2):

$$\phi(x) = \phi_0 = \left(\frac{-\mu^2}{2\lambda}\right)^{\frac{1}{2}} e^{i\theta}, \quad 0 \le \theta < 2\pi \quad (1.25)$$

where the phase angle θ defines a direction in the complex ϕ-plane. Thanks to the invariance, gauge freedom allows to choose $\theta = 0$, leading to the *real* value $\phi_0 = \left(\frac{-\mu^2}{2\lambda}\right)^{\frac{1}{2}} \equiv \frac{1}{\sqrt{2}} v \ (> 0)$.

At the end, the original scalar field $\phi(x)$ can be expressed as a real field in a perturbative expansion of the chosen minimum:

$$\phi(x) = \frac{1}{\sqrt{2}}[v + \sigma(x)] \quad (1.26)$$

At this point we can say that symmetry of $\mathscr{V}(\phi)$ has been removed and the ground states has *broken* the symmetry. Substituting 1.26 in 1.24 gives a form like $\mathcal{L}(x) = \mathcal{L}_0(x) + \mathcal{L}_I(x)$:

$$
\begin{aligned}
\mathcal{L}(x) &= \frac{1}{2}(\partial_\mu \sigma(x))(\partial^\mu \sigma(x)) - \frac{1}{2}(2\lambda v^2)\sigma^2(x) \\
&\quad - \frac{1}{4}F_{\mu\nu}(x)F^{\mu\nu}(x) + \frac{1}{2}(qv^2)A_\mu(x)A^\mu(x) \\
&\quad - \lambda v \sigma^3(x) - \frac{1}{4}\lambda \sigma^4(x) \\
&\quad + \frac{1}{2}q^2 A_\mu(x)A^\mu(x)[2v\sigma(x) + \sigma^2(x)] \quad (1.27)
\end{aligned}
$$

The interpretation of the 1.27 terms brings to some crucial considerations. The first two lines are $\mathcal{L}_0$, where we have a free scalar field $\sigma(x)$ with a mass $M_H = \sqrt{2\lambda v^2}$ and a *massive* vector field $A_\mu(x)$ of mass $|qv|$ replacing the initial massless gauge field. The second two lines represents the $\mathcal{L}_I$, with self-interaction of the scalar field and the interaction with the vector field with coupling strengths of $q^2 v$ and $\frac{1}{2}q^2$.

What we got is just the *spontaneous symmetry breaking* coming from the assignment of one initial degree of freedom of ϕ to the vector field A_μ, which then acquires mass. The massive spin 0 boson associated with the field $\sigma(x)$ is called *Higgs boson*.

Symmetry breaking in SM

Since electro-weak theory is $SU(2) \otimes U(1)$ gauge invariant, the Higgs mechanism must be adapted to such a symmetry group in order to produce the lepton and boson masses and finally arrive to the Weinberg and Salam formulation [14]. In the following a brief description of the procedure is given. The basic idea is to introduce again an *Higgs field* that can break U(1) as well as $SU(2)$ symmetry, so we use a weak isospin doublet made by two scalar fields:

$$\Phi(x) = \begin{pmatrix} \phi_a(x) \\ \phi_b(x) \end{pmatrix} \tag{1.28}$$

The 1.28 transforms as 1.10 under $SU(2) \otimes U(1)$ gauge transformations. Including the Higgs field and its interactions with boson and lepton fields in the electro-weak Lagrangian, we obtain a generalized form as:

$$\mathcal{L} = \mathcal{L}^L + \mathcal{L}^B + \mathcal{L}^H + \mathcal{L}^{HL} \tag{1.29}$$

As a next step one defines the vacuum state energy. The particular value:

$$\Phi_0 = \begin{pmatrix} \phi_a^0 \\ \phi_b^0 \end{pmatrix} = \begin{pmatrix} 0 \\ v/\sqrt{2} \end{pmatrix} \tag{1.30}$$

where $v = (-\mu^2/\lambda)^{1/2}$, is chosen for the ground state, so that we derive the Higgs field as $\Phi(x) = \frac{1}{\sqrt{2}} \begin{pmatrix} 0 \\ v+\sigma(x) \end{pmatrix}$, as in 1.26. Since the process began with a doublet of complex scalar fields and finished with a real doublet, we can say that in the Lagrangian three degrees of freedom are absorbed by the $W^\pm, Z$ bosons to acquire mass, while the photon remain massless as desired and the scalar massive Higgs boson comes from $\sigma(x)$, with a mass $M_H = \sqrt{2\lambda v^2}$ that is a free parameter to be measured experimentally.

Lepton and quark masses are assumed to arise from Yukawa interactions with the scalar Higgs. They are directly proportional to Yukawa coupling constants $Y_{q,l}$ and are expressed, in lepton case, in $\mathcal{L}^{LH}$ part:

$$
\begin{aligned}
\mathcal{L}^{LH}(x) &= -Y_l[\bar{\Psi}_l^L(x)\psi_l^R(x)\Phi(x) + \Phi^\dagger\bar{\psi}_l^R(x)\Psi_l^L(x)] \\
&\quad -Y_{\nu_l}[\bar{\Psi}_l^L(x)\psi_{\nu_l}^R(x)\tilde{\Phi}(x) + \tilde{\Phi}^\dagger\bar{\psi}_{\nu_l}^R(x)\Psi_l^L(x)]
\end{aligned}
\tag{1.31}
$$

where $\tilde{\Phi}(x) = -i[\Phi^\dagger(x)\tau_2]^T$. The masses are introduced as parameters to be experimentally measured, derived from coupling constants and the Higgs field:

$$
m_l = Y_l\frac{v}{\sqrt{2}}
\tag{1.32}
$$

For quarks, we must take in account that also upper member of quark doublet must have mass. To acquire this feature the Higgs doublet is re-constructed as $\Phi_c = -i\tau_2\Phi^*(x)$ and an hermitian conjugate member is added to the lagrangian. It is interesting to observe that, since the vacuum expectation value of the Higgs field is $v = 246$ GeV, the Top quark Yukawa coupling is:

$$
Y_t = \frac{m_{\text{top}}\sqrt{2}}{v} \sim 1
\tag{1.33}
$$

1.2 Higgs Boson Physics

1.2.1 Production mechanisms at particle colliders

In the Standard Model, since the coupling of the Higgs boson to fermions and bosons is proportional to their mass, the cross sections for associated production to top quark and to W, Z heavy bosons are relatively large. The four main production processes are thus: the gluon-gluon fusion mechanism; $gg \to H$ via top quark loop, the associated production with W/Z bosons: $q\bar{q} \to V + H$, the weak vector boson fusion processes: $qq \to V^*V^* \to qq + H$ and the associated Higgs production with heavy top or bottom quarks $gg, qq \to tt/bb + H$. Of these production mechanisms, associated production with W/Z bosons is the most suitable for searching for invisible decaying Higgs boson at Tevatron. While the gluon-gluon fusion production cross section is the largest, these events are undetectable because the only particles in the final state would be the invisible daughters of the Higgs boson. Associated production with W/Z bosons has the next highest cross section, and unlike in gluon-gluon fusion production, the final state can include the visible decay products of the W/Z boson.
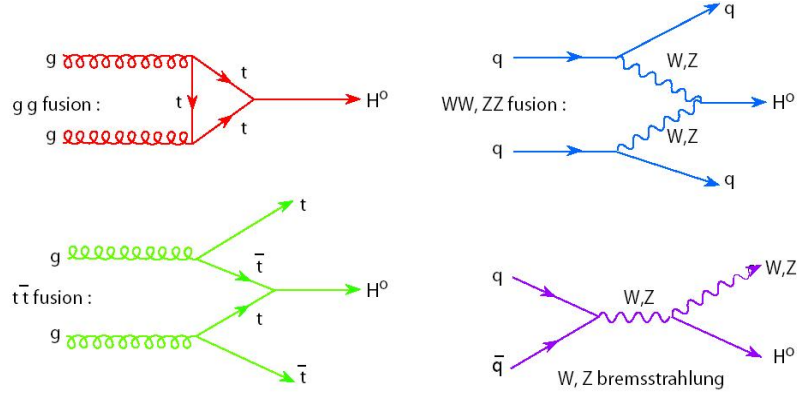
Figure 1.3: (a) gluon-gluon fusion, (b) associated production with vector boson,(c) vector boson fusion, (d) associated production with heavy quarks.
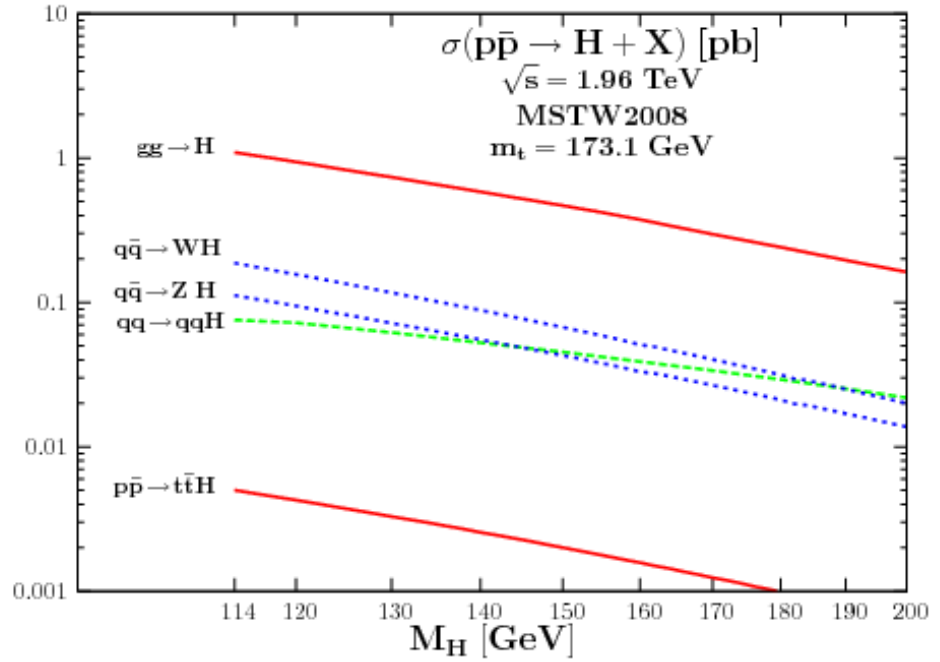

Figure 1.4: Predictions for Higgs production at the Tevatron and the associated uncertainties

In Fig. 1.3 the leading order Feynman diagrams of Higgs production are shown, and the cross sections for these production mechanisms at Tevatron for $\sqrt{s} = 2TeV$, are shown in Fig. 1.4.

The $Z \to b\bar{b}$ decay channel must also be considered in the associated production with the Z boson. The advantage of this channel is the larger branching fraction of $Z \to b\bar{b}$ compared to $Z \to \ell^+\ell^-$. The disadvantages are the lower efficiency for identifying $b\bar{b}$ final states compared to leptonic final states, the reduced Z boson invariant mass resolution, and the more difficult background sources. These backgrounds include contributions from ZZ, WZ, $Zb\bar{b}$, $Wb\bar{b}$, single top, and tt production. The significance of the $Z \to b\bar{b}$ channel is not as high as in the lepton channel, but this channel could be combined with the lepton channel, or be used to confirm an observed signal. The potential background to such type of associated production with the Z boson is $Z \to \nu\nu$ u and $H \to b\bar{b}$. The Z(vv)H(bb) background is negligible and not included, because we require isolated charged leptons in the final state.

1.2.2 Decays of light SM Higgs boson

In the SM the decay modes dominant for a Higgs boson of mass 125 GeV/c^2 are $H \to b\bar{b}$ and $H \to WW^*$, followed by $H \to gg$, $H \to \tau^+\tau^-$, $H \to c\bar{c}$ and $H \to ZZ^*$. With much smaller rates follow the decays $H \to \gamma\gamma$ $H \to \gamma Z$ and $H \to \mu^+\mu^-$.
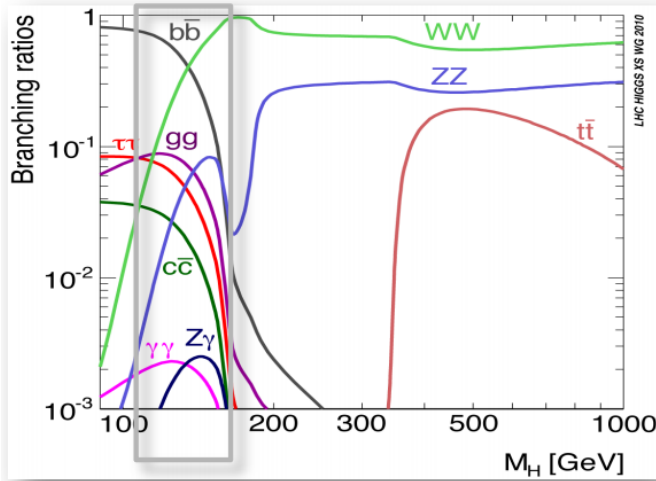
Figure 1.5: Branching ratios of the SM Higgs boson decay as a function of the Higgs boson mass [17].

The Higgs decays into WW^* and ZZ^* effectively need to be studied considering the decays of the gauge bosons into four fermions, i.e., the leptonic, semi-leptonic and full hadronic final states.

Decay channels	Branching fractions	Rel. uncertainty
$H \rightarrow \gamma\gamma$	2.3×10^{-3}	$\pm 5.0\%$
$H \rightarrow ZZ$	2.65×10^{-2}	$\pm 4.2\%$
$H \rightarrow W^+W^-$	2.15×10^{-1}	$\pm 4.15\%$
$H \rightarrow \tau^+\tau^-$	6.3×10^{-2}	$\pm 5.7\%$
$H \rightarrow b\bar{b}$	5.8×10^{-1}	$\pm 3.3\%$
$H \rightarrow \gamma Z$	1.5×10^{-3}	$\pm 9.0\%$
$H \rightarrow \mu^+\mu^-$	2.2×10^{-4}	$\pm 6.0\%$

Table 1.2: Main Higgs decay channel and the associated branching fraction (from [7]).

Such a light SM Higgs boson couples only very weakly to all off-shell states, and has a narrow decay width which for $H \rightarrow f\bar{f}$ depends on the squared coupling m_f^2/v^2 , where v = 175 GeV. The largest mass fermion pair that Higgs boson can decay into is the b quark with $m_b \approx 4.5$ GeV, leading to a squared coupling of order $m_b^2/v^2 \approx 10^{-3}$.
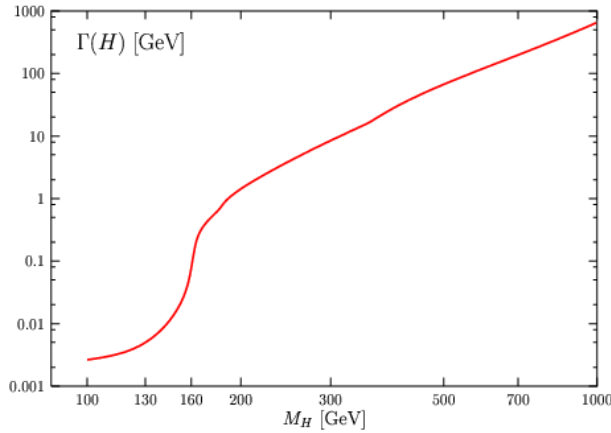
Figure 1.6: Total decay width of the SM Higgs boson decay as a function of the Higgs boson mass [17].

The Higgs boson couples to physical gauge bosons after EWSB through the covariant derivative of Higgs field $D_\mu\Phi$. The Higgs boson couples to fermions through the Yukawa coupling in the $SU(2)_L + U(1)_Y$ Lagrangian with coupling strength m_f/v. Thus the Higgs can only decay directly to gauge boson pairs or fermion pairs through a point interaction. Coupling strengths of

$H \to VV^*$ and $H \to f\bar{f}$ are proportional to $m_H M_V^2$ and $m_f^2 m_H$, respectively.

The branching ratios for the most relevant decay modes of the SM Higgs boson as functions of m_H are shown in Fig. 1.5 and and listed for $m_H = 125$ GeV$/c^2$

1.3 Invisible Higgs decay

Given the discovery of a Higgs boson, it is now an important task to measure its properties to test its consistency with the standard model. The properties of the standard model Higgs are precisely known, and so such measurements serve as a window to physics beyond the standard model (BSM).

One such property is the Higgs decay width. In the SM, the width of the Higgs boson is calculated to be $\Gamma_H = 4$ MeV. Intrinsic detector resolution is on the order of a few GeV in the channels that can be measured best. Therefore, direct limits are inherently weak, with $\Gamma_H{}^{MAX} \approx 1000\Gamma_H{}^{SM}$, leaving room for Physics Beyond the Standard Model (BSM).
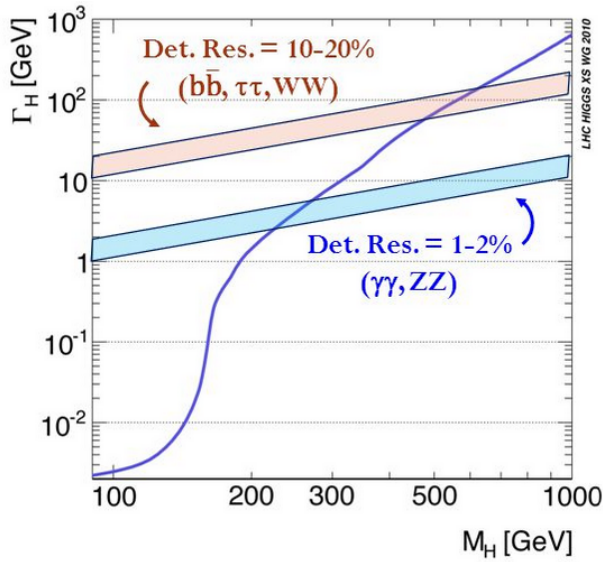
Figure 1.7: Observed Higgs width uncertainties dominated by detector resolution at low mass, while the uncertainties on the Higgs width becomes a broad resonance dominated by the *natural width* at high mass

1.3.1 Invisible Higgs Production Mechanism

The vector boson-vector boson fusion process ($qq \to qqV^*V^* \to qH$) has the smallest production cross section, but even so has recently been shown to be a viable channel for triggering and searching for Higgs boson invisible decays [16].

The associate production of Higgs bosons with W or Z bosons, known as Higgs-strahlung, is an important search channel for Higgs bosons at the Tevatron for low Higgs-boson masses. Associated production with the W boson occurs via $q\bar{q} \to W^* \to WH$, which is followed by $W \to \nu l$ and $H \to inv.$. This type of event is easy to trigger since it produces a clean EM signal, has a significant missing transverse momentum, and moreover the lepton due to off-shell-produced W^* which decay leptonically possesses a high transverse momentum. However, background due to off-shell W^* production which decays leptonically is irreducible even after the kinematical cuts [18].

A more exploitable channel is associated production with the Z boson, $q\bar{q} \to Z^* \to ZH$. There is an irreducible background for the above process from ZZ production, where one Z boson decays leptonically and the other Z boson decays into neutrinos. Since ZZ is produced by t-channel processes, it is expected that the P_T distribution of the Z bosons will be softer than the P_T distribution of the Z bosons from the ZH s-channel production process. For this reason the kinematic distribution of the final state can be used in order to discriminate this process to our signal. The next most significant irreducible background is from WW production with each W decaying leptonically. This background has a considerably softer transverse momentum distribution. Since these backgrounds have softer transverse momentum distributions than the signal, it might be possible to detect a signal by requiring high missing transverse energy. Other backgrounds arise from WZ, Wj, and $Z^* \to \tau^+\tau^- \to \ell^+\ell^- + \not{E}_T$, but they can be suppressed.

1.3.2 Invisible Higgs Decay

The Higgs decay width to invisible particles serves as a sensitive probe of BSM physics because the standard model value, dominated by the H $\to ZZ^*$ $\to 4\nu$ decay, is small. The presence of massive, invisible BSM particles could significantly increase this width.

The invisible Higgs decay channel is also important in the search for additional Higgs bosons. While additional SM-like Higgs bosons have been excluded over a wide range of masses, those with exotic decay modes remain a possibility.

Detection is difficult for particles with small couplings, but their presence can still be inferred from the energy and momentum they carry away from an interaction, as is done for neutrinos. Detection is also difficult if particles are massive and quickly decay into ordinary quarks and leptons. Only by reconstructing all the decay products in a large set of collisions (or events) can the parent particle be inferred.

Up to now it has been generally assumed that only SM particles are present in

the Higgs decays, however there are many BSM scenario in which the Higgs coupled to new particles, that can enhance the Higgs boson decay branching fractions. The new states could happen to not be detectable, resulting in missing transverse energy in our detector. The list of some of the possible types of invisible Higgs decays follows.

- Higgs boson decays to neutralinos [[19]]

- Higgs boson decays to neutrinos in extra dimensions [[20, 21]]

- Higgs boson decays to Majorons [[22, 23]]

- Standard Model with an extra singlet

Standard Model with an extra singlet (Dark Matter interpretation)

In this model there exists one gauge-singlet scalar boson $S = S_0 + iA_0$ and one doublet Higgs boson whose vacuum expectation values constitute all of EWSB symmetry breaking, and which therefore couples to the W and Z bosons with the same strength as the SM Higgs boson. If $S = 0$ there is no mixing between the S and the H, and if $m_S < m_H/2$ then $H \to S_0 S_0, A_0 A_0$ are allowed with couplings derived in [26]. Since the S_0 does not mix with the H there will be no suppression of ZH production. Also, since S has no couplings to SM gauge bosons or fermions, it will be stable and invisible to the detectors.

1.3.3 Search in associated ZH production

Only by reconstructing all the outgoing secondary decay products in a large set of collisions (or events) can the parent particle be inferred.

An Higgs boson decaying invisibly can have a clear signature in the associated ZH production mode.

In fact, no matter how crazy and untriggerable the Higgs decay is, the decay of the W or Z in these collisions will ensure that data at least 1% of the exotic Higgs decays will be recorded.
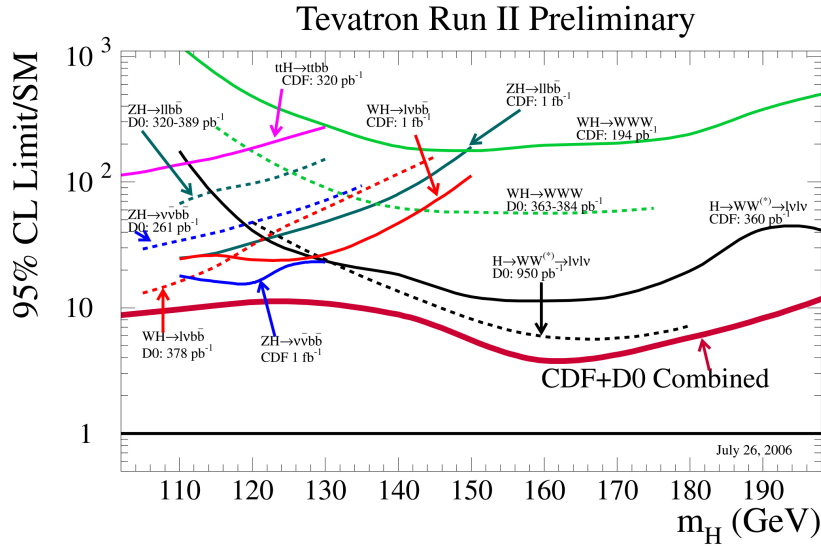
Figure 1.8: Higgs production at the Tevatron

In the associated production with a vector boson, the ZH process with $Z \to \ell\ell$ has been identified to be the most promising one in the invisible Higgs search[27], because despite the fact that the WH channel has a larger cross section (as it can be seen in Fig. 1.8), this process is dominated by the strong background from the leptonic W-decay.

The $q\bar{q} \to Z^* \to ZH$ process instead, with $Z \to \ell\ell$, as shown in Figure [1.9], provide the cleanest signatures for detection at hadron collider experiments because of the very small expected background.

Other processes that do not involve the Higgs can also result in a two-lepton plus $\not{E}_T$ final state.
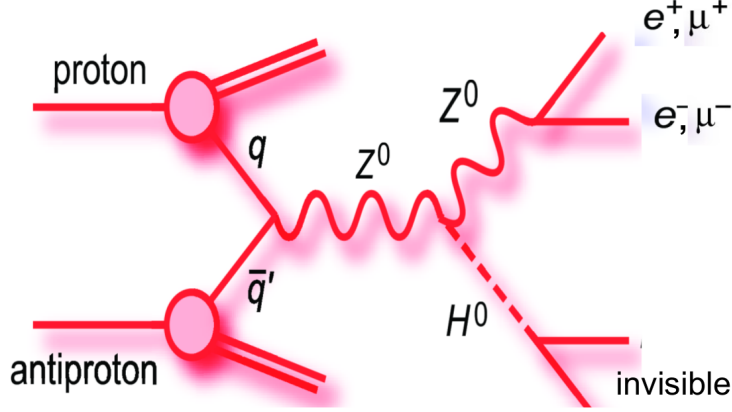
Figure 1.9: Higgs production at the Tevatron

In particular diboson ZZ production is the dominant background: $ZZ \rightarrow \ell\ell\nu\nu$ where both bosons decay leptonically. The simplest $H \rightarrow$ invisible process is highly suppressed in the SM. However, beyond-the-SM scenarios allow for enhanced $H \rightarrow$ invisible decay rates that are potentially observable by collider experiments. In this analysis, we search for a $H \rightarrow$ invisible process in the ZH associated production mode. Despite the suppressed cross section relative to direct H production by gluon fusion, the ZH production mode allows one to trigger on leptonic decays of the Z. For this analysis, we reconstruct Z candidates from the e^+e^- and $\mu^+\mu^-$ dilepton four-momenta. We do not explicitly reconstruct $Z \rightarrow \tau^+\tau^-$ processes. However, we still gain some acceptance from $\tau^+\tau^-$ decays to same-flavor final states. Events with $e^\pm\mu^\mp$ pairs are used as a control region to test background modeling, as well as events with same-sign, same-flavor lepton pairs. The event selection is described later in Ch. 4.

Current status

Up to now, the ATLAS collaboration has set the most stringent condition on the low-mass DM candidates from the invisible Higgs decays (see Fig. [?]). They have undertaken a search for invisible decays of a Higgs boson produced in association with a Z boson. The distribution of the missing

transverse energy $\not{E}_T$ in events with an electron or a muon pair consistent
with a Z boson decay is used to constrain the $\sigma_{ZH} \times BR(H \to inv.)$, over
the mass range $110 < m_H < 400$ GeV. To set an upper limit on the invisible
Higgs production cross-section, mass of the Higgs boson is taken to be $m_H =$
125.5 GeV, the best-fit value from the ATLAS experiment, and the ZH
production cross section is assumed to be that predicted for the SM Higgs
boson. This assumption implies that the hypothesized unobserved particles
that couple to the Higgs boson have sufficiently weak couplings to other SM
particles to not affect the Higgs boson production cross sections. The SM
branching ratio of the Higgs boson decaying to invisible particles is 1.2×10^{-3}
and arises from the $H \to ZZ^* \to 4\nu$ decay. The present search at colliders
is not sensitive to the low branching ratio for this decay, so Atlas searches
for enhancements in the decay fraction to invisible particles due to physics
beyond the Standard Model (BSM). They have set the limits on the cross
section times branching ratio for a Higgs boson decaying to invisible particles
anywhere in the full mass range . The limits have been computed using a
maximum likelihood fit to the $\not{E}_T$ distribution following the signal confidence
level modified frequentist formalism [28] with a profile likelihood test statistic,
see Fig. [1.10].
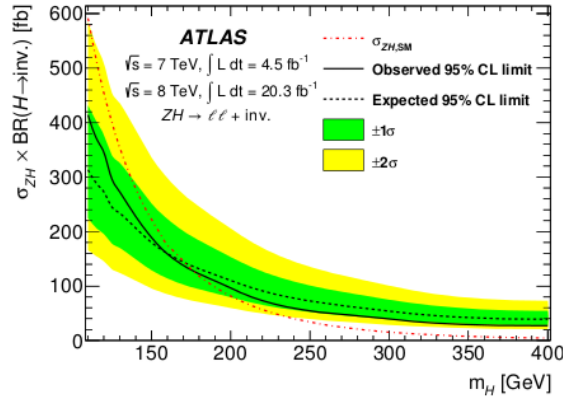
Figure 1.10: Observed 95% C.L. upper limits on $\sigma_{ZH} \times BR(H \to inv.)$ for
the combined 7 and 8 TeV data at LHC (Atlas collaboration). The full and
dashed lines show the observed and expected limits, respectively [29].

Chapter 2

The CDF Detector at Tevatron

2.1 The Tevatron Collider

The Tevatron was a proton-antiproton accelerator and collider located at the Fermi National Accelerator Laboratory in Batavia, Illinois. Proton and antiproton production, several stages of acceleration, and antiproton storage are performed with a chain of accelerators.
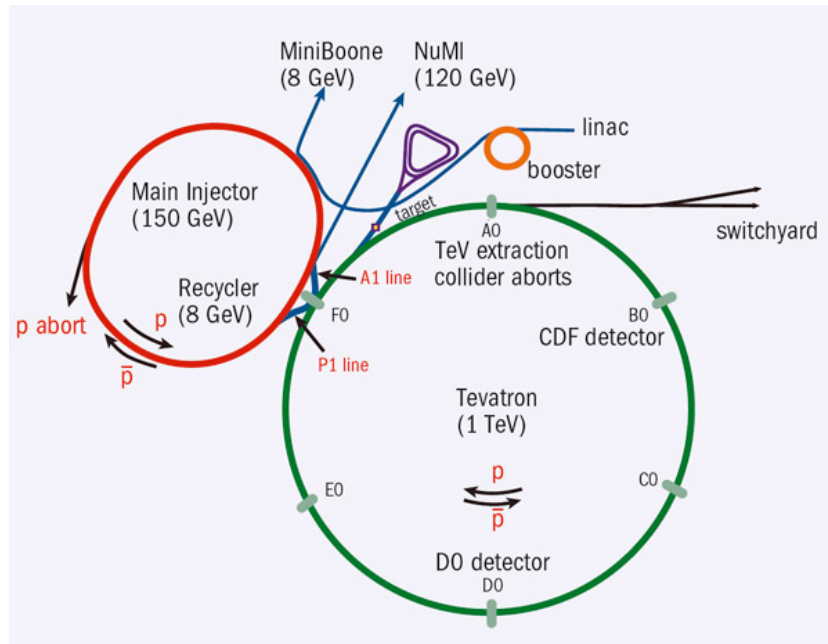
Figure 2.1: The Fermilab accelerator system.

This complex of accelerators that ultimately inject proton and antiproton beams into the Tevatron ring are shown in Fig. 2.1. Collisions occur at a

center-of-mass energy of $\sqrt{s} = 1.96$ TeV, which before the start of LHC was the highest energy $p\bar{p}$ collisions ever produced in a laboratory, at two interaction points. The Collider Detector at Fermilab (CDF) and D0 detectors were located at these interaction points.

2.1.1   The Proton Source

The Tevatron proton beam originates from negatively ionized hydrogen atoms (H^-) which in the first realization of the source were bought to the energy of 750 keV with a Cockroft-Walton accelerator. Next, the H^- ions are accelerated to an energy of 400 MeV in LINAC, a 150 m long series of radio-frequency (RF) cavities. The H^- ions are then passed through a carbon foil that strips the electrons off, leaving protons that are injected into the Booster, the next accelerator in the complex. The Booster is a synchroton accelerator that increases the protons' energy to 8 GeV using RF cavities. After leaving the Booster, the protons enter the Main Injector, a 3 km in circumference synchrotron that brings their energy to 150 GeV before injection into the Tevatron.

2.1.2   The Antiproton Source

Antiprotons are produced by directing a 120 GeV proton beam from the Main Injector onto a Nickel alloy target. The products of the collisions with the target, which include antiprotons, are focused into a beam using a magnetic lithium collection lens, and the antiprotons are selected with a charge-mass spectrometer. The selected antiprotons are sent to the Debuncher storage ring, which removes the bunch structure created by the incident protons and reduces large momentum spread. The latter is achieved with the stochastic cooling technique, which, in a feedback mechanism, measures deviations of the bunch from the ideal orbit with a set of electrostatic plates and then applies a correction with electrostatic plates downstream. This results in the reduction of transverse momentum and energy spread without beam loss. The Debuncher delivers an 8 GeV antiproton beam to the Accumulator storage ring that stores the antiprotons until all Debuncher cycles are complete. When the Accumulator is saturated, they are transferred to the Recycler, a second storage ring made from permanent magnets. The recycler has a larger acceptance than the accumulator and further reduces the size and spread of the beam using an electron cooling technique where a beam of electrons travels along with the antiprotons and absorb energy. Once a sufficient number of antiprotons are available in the recycler, they are injected into the main

injector, which increases their energy to 150 GeV. Finally, the antiprotons are injected into the Tevatron in the opposite direction of the proton beam.

2.1.3 Luminosity and Tevatron Performance

Instantaneous luminosity is defined as the interaction rate per unit cross section of the colliding beams (collisions/(cm^2·s)). In the absence of beam offsets or a crossing angle, instantaneous luminosity is given by

$$\mathcal{L} = \frac{f_{\text{rev}} n_b N_p N_{\bar{p}}}{2\pi(\sigma_p^2 + \sigma_{\bar{p}}^2)} F\left(\frac{\sigma_l}{\beta^*}\right),$$
(2.1)

where f_{rev} is the revolution frequency, n_b is the number of bunches, $N_{p(\bar{p})}$ is the number of protons (antiprotons) per bunch, and $\sigma_{p(\bar{p})}$ is the transverse proton (antiproton) beam size at the interaction point. F is a factor that depends on the beta function value at the interaction point, a measure of the local transverse beam size commonly referred to as β^*, and the bunch length σ_l. The history of peak instantaneous luminosity is shown in Fig. 2.2. In Run II, Tevatron delivered 12 fb^{-1} of data per experiment.
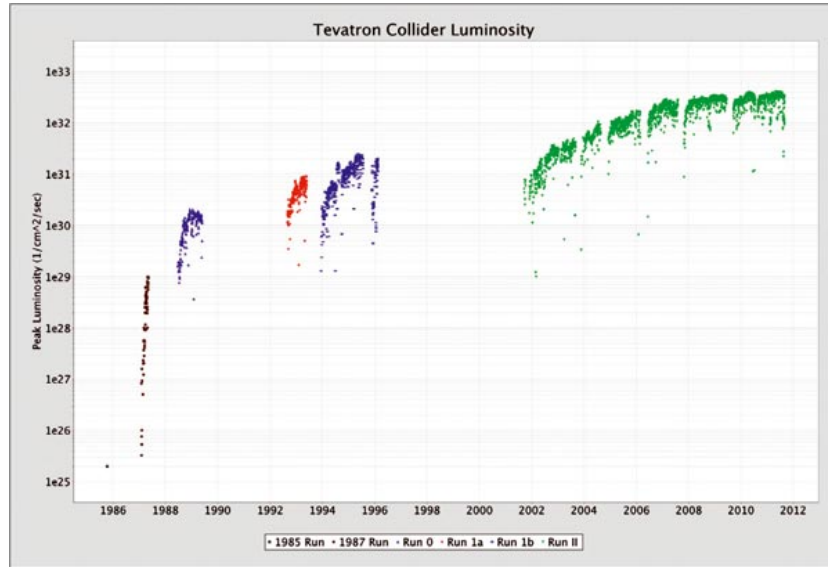
Figure 2.2: Tevatron integrated luminosity as a function of Run II weeks (left) and peak luminosity as a function of calendar date (right). Empty regions correspond to Tevatron shut-down periods.

2.2 The CDF detection system

The CDF experiment is a part of the Tevatron accelerator complex, supplied by the $p, \bar{p}$ luminosities of up to $1. \times 10^{23}$ cm^{-2} s $^{-1}$ and operating at the energies of $\sqrt{s} \sim 2$ TeV. The CDF II detector is a multipurpose solenoidal spectrometer (see Fig. 2.3) surrounded by calorimeters and muon detectors [30, 31]. The geometry of the overall detector is described using the azimuthal angle ϕ and the pseudorapidity $\eta = -\ln[\tan(\theta/2)]$, where θ is the polar angle with respect to the proton beam axis (positive z-axis). The origin of the z-axis is taken at the $p\bar{p}$ interaction point. In the Run II configuration comprises:

- a **tracking system**, which comprises three silicon microstrip trackers (L00 , SVX and ISL) and an open-cell drift chamber (COT) inside a superconducting solenoid, that provides a constant 1.4 T magnetic field parallel to the beam direction, with the purpose of bending into helixes the trajectories of charge particles to allow determining their momentum and charge;

- a **Time of Flight** system (TOF), located outside the COT , for measuring the mass of charged particles with momenta up to 2 GeV/c ;

- a **calorimeter system**, with the purpose of measuring the energy of charged and neutral particles;

- **muon chambers and scintillators**, used to track and identify muons, that pass through the calorimeters interacting as minimum ionizing particles (m.i.p.);

- **luminosity monitors**, for the instantaneous luminosity measurement, necessary to derive cross section from event yields.

2.2.1 Coordinates system and standard definitions at CDF

A left-handed Cartesian coordinate system is used, where the origin is defined to be at the nominal Bø interaction point. The z -axis points along the nominal beam line in the direction of the proton beam. The y -axis points vertically upward, and the x -axis points radially outward from the center of the Tevatron. A cylindrical coordinate system (r , ϕ , z) is also used, where

$$r = \sqrt{x^2 + y^2} \quad \text{and} \quad \phi = \tan^{-1} \frac{y}{x} \ . \tag{2.2}$$
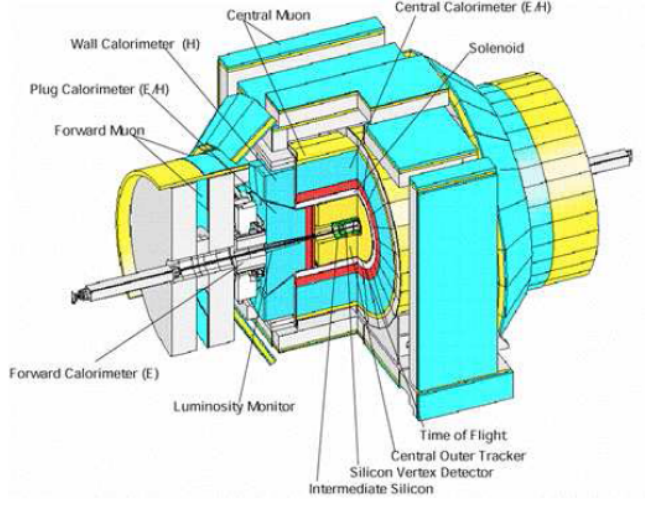
Figure 2.3: The CDF II detector [32].

Pseudorapidity is defined as

$$Y \xrightarrow{p \gg m} \eta = -\ln\left(\tan\frac{\theta}{2}\right) \tag{2.3}$$

where $\theta = \tan^{-1}\frac{\sqrt{x^2+y^2}}{z}$.

The spatial separation between particles in the detector is commonly given in terms of a Lorentz invariant variable defined as:

$$\Delta R = \sqrt{\Delta\phi^2 + \Delta\eta^2}. \tag{2.4}$$

Other quantities useful to describe the kinematics of $p\bar{p}$ interactions are the transverse momentum and the transverse energy, defined as $p_T = p\,\sin\theta$ and $E_T = E\,\sin\theta$, respectively.

2.2.2 Central tracking system

The CDF central tracking system consists of silicon detectors and a drift chamber situated inside a solenoid that provides a 1.4 T magnetic field coaxial with the beam. The silicon microstrip detector has eight cylindrical layers of mostly double-sided silicon, distributed in radius between 1.5 cm and 28 cm. The system is read out in about 700.000 channels and can provide three-dimensional precision tracking up to $|\eta| < 2.0$. Layers are grouped in three components: L00, SVXII, and ISL. Layer zero-zero (L00) is a single sided,

radiation tolerant silicon strip detector, which is closest to the beamline. It is 87 cm long, centered on $z = 0$, and has a radius of just 1.1 cm. L00 is constructed in six segments in both z and ϕ. Each ϕ segment contains 128 channels of narrow inner sensors and 256 channels of wider outer sensors. Each z segment is composed of two long sensors. In total, L00 contains 13,824 channels. The SVX II silicon detector encapsulates L00. It is composed of three barrels, positioned end-to-end to achieve a length of 81 cm and full coverage in ϕ. Each barrel contains five layers of silicon microstrip detectors ranging from 2.4 cm to 10.6 cm from the beamline. In all, the SVX contains 405,504 detection channels. The "intermediate silicon layers" (ISL) are the outermost section of the silicon detector system, between the SVX and the central outer tracker (COT). The ISL are an important complement to the SVX and COT in that they provide extra tracking information in $1.0 < |\eta| < 2.0$, where COT coverage is partial. In this forward region, there are two silicon layers placed at 20 cm and 28 cm from the beamline. There is also an additional ISL layer in the central region at 22 cm from the beamline. The structure of the central tracking system is given in Fig. 2.4
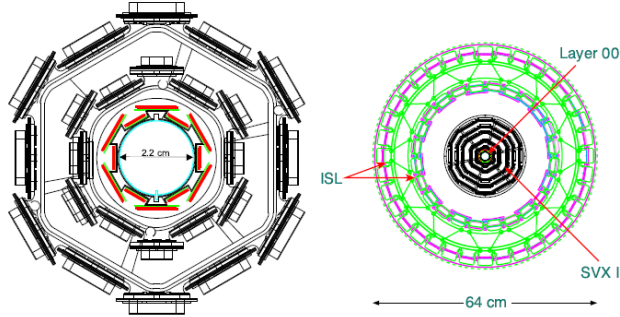
Figure 2.4: End view of L00 (left) and the full silicon system (right) [32].

Outside of the silicon detectors and for $|\eta| < 1.0$, charged particles are detected by the central outer tracker, an open-cell drift chamber (COT). The number of COT layers traversed by a particle in the range $|\eta| \leq 1$ is 96 and decreases to zero for $|\eta| \rightarrow 2$. It covers the comparatively larger range of 40 cm to 130 cm from the beamline and is approximately three meters long. The 96 layers are partitioned into 8 "superlayers" alternating between axial and stereo. "Axial" layers provide hit coordinates in the transverse plane (radial and azimuthal angle) while "stereo" layers supply the z coordinate, together yielding hit information in three dimensions. The COT is filled with an equal mixture of argon and ethane. When a charged particle enters the COT

apparatus, it ionizes the gas by creating e^+e^- pairs. Electrons then drift toward anode wires, and signals are induced from the flow of charge.

2.2.3 Electron/hadron calorimetric system

Inside the solenoid, a scintillator-based time-of-flight detector allows particle electromagnetic and hadronic shower identification with a timing resolution of about 100 ps. Electromagnetic calorimeter showers are induced for high energy photons and electrons via a combination of bremsstrahlung and pair production. When impinging on the heavy metal layer, a high energy electron will radiate high energy photons, which then converts to e^+e^- pairs, which go on to emit more photons, etc. This cycle continues until the individual photons and electrons no longer have enough energy to produce pairs and the ionization loss prevents further radiation. Hadronic showers occur when a high energy hadron experiences an inelastic nuclear collision with the heavy metal layer, producing secondary hadrons that go on to have their own collisions. This cycle continues until the individual hadrons no long have enough energy to generate significant ionization in the medium. Hadrons tend to be much more massive than electrons and a relatively large amount of energy is released from nuclear interactions, so the depth that a hadronic shower penetrates is larger and such calorimeters must be physically larger than the electromagnetic calorimeters, as shown in Fig 2.5. The combined elec-
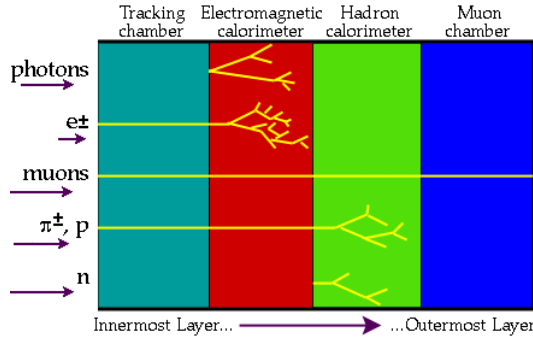
Figure 2.5: How various particles show up at CDF.

tromagnetic and hadronic calorimeters (EM and HAD) are lead-scintillator (front) and iron-scintillator (rear) sampling calorimeters, providing coverage at $|\eta| \leq 3.6$ in a segmented projective tower geometry. At depths corresponding to one hadronic-interaction length (λ), which is equivalent to 18-20 radiation lengths (X_0), lead absorber is used to measure the electromagnetic component of showers, while in the region $4.5 - 7\lambda$ iron is used to contain the hadronic component.

The central calorimeter in total covers the pseudorapidity region $|\eta| \leq 1.1$. Electromagnetic component of it (CEM) is composed of 48 wedges that each cover 15 ° in azimuth and 0.11 in pseudorapidity (η). Each 15 ° wedge has alternating lead and scintillator layers. The forward calorimeter extends the coverage into the region $1.1 \geq |\eta| \leq 3.6.$. The central hadronic calorimeter (CHA) and the endwall hadronic calorimeter (WHA) wedges are composed of alternating layers of iron and scintillator. Both the CHA and WHA are an array of 48 wedges, with the CHA covering $|\eta| < 0.9$ and the WHA covering $0.7 < |\eta| < 1.3$. The forward calorimeters are also divided in a "plug electromagnetic calorimeter" (PEM) and a "plug hadronic calorimeter" (PHA), covering $1.1 < |\eta| < 3.6$ and $1.2 < |\eta| < 3.6$ respectively. The forward calorimeter extends the coverage into the region $1.1 \geq |\eta| \leq 3.6.$.

2.2.4 Shower maximum detectors

Proportional wire and scintillating strip detectors (SMX) are embedded in the electromagnetic calorimeters at a depth of approximately $6X_0$ corresponding to the electromagnetic shower maximum and provide measurements of the transverse shower profile at $|\eta| \leq 2.8$. In this manner they assist in the position measurement and background suppression for electrons. In addition, an early energy sampling is obtained using preradiator chambers positioned between the solenoid coil and the inner face of the central calorimeter.

2.2.5 Muon tracking system

Outside of the calorimeter and behind additional steel absorbers, a multilayer system of drift chambers and scintillation counters allows detection of muons covering $|\eta| \leq 1.5$. Since muons are to a good approximation minimum ionizing particles, they deposit only a small fraction of their energy in the absorbers.

The four muon detector components used are the "Central MUon chambers" (CMU), "Central Muon uPgrade" (CMP), and the "Central Muon eXtension" (CMX) and "Intermediate MUon" (IMU) system in the forward region of the detector ($|\eta| > 1.0$), which contains the "Barrel MUon" chamber (BMU) and BSU/TSU scintillators. The CMP and CMX muon detectors contain two systems: a stack of four single-cell drift chambers that provide a short track called a "stub" and a scintillation counter. The CMU has only a drift chamber. These detectors are used in tandem with the silicon and COT trackers to establish muon tracks from which the transverse momentum P_T is gauged by the track curvature. Since this analysis focuses on a signal with a leptonic
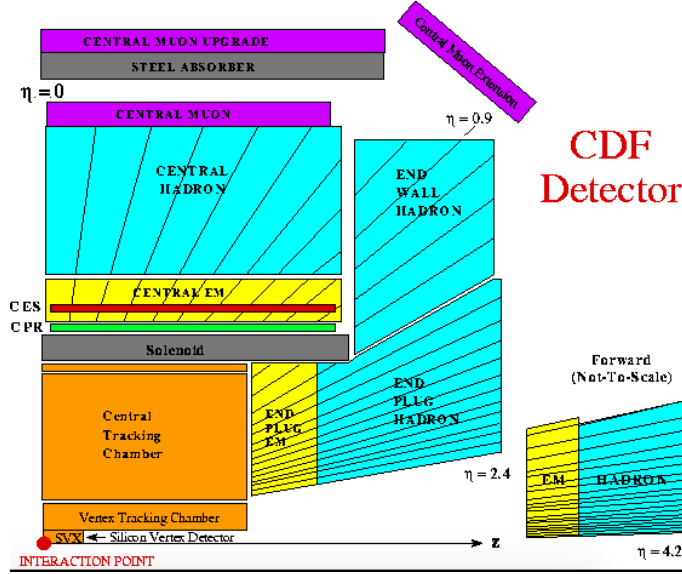
Figure 2.6: Diagram showing a side view of the tracking, solenoid, and forward calorimeter systems [32].

signature, the detection of muon (along with electrons) is critical to finding, excluding, or setting limits on a signal.

2.2.6   The CDF Trigger System

$p\bar{p}$ collisions at Tevatron happen with a frequency of 2.5 MHz (i.e every 396 ns). The bunch-bunch luminosity and the interaction cross-section are such that in average one or a few interactions take place at each bunch crossing. With an average event size of $\sim$ 250 kb, this represents a huge amount of data which would flow through the CDF data acquisition system (DAQ). The CDF DAQ can sustain only a small fraction of this data flow, since the maximum rate for storing data to disk is $\sim$ 75 Hz.

The trigger is the system devoted to perform a quick online selection and keep only the events interesting for physics. A rejection factor of 10000 is needed to match the DAQ capabilities. As shown in Fig. 2.7, the CDF trigger is implemented in three levels of successively tighter and more sophisticated event selection. The first level is hardware based; the second is a mixture of hardware and software, and the third is purely software, implemented in an on-line computer cluster. At LEVEL 1 the selection algorithms are hard-coded into the electronic circuits of the trigger boards. In a synchronous pipeline up to 42 subsequent events can be stored for $\sim$ 5.5 μs while the logic is making a decision. If no acceptance decision is made within that
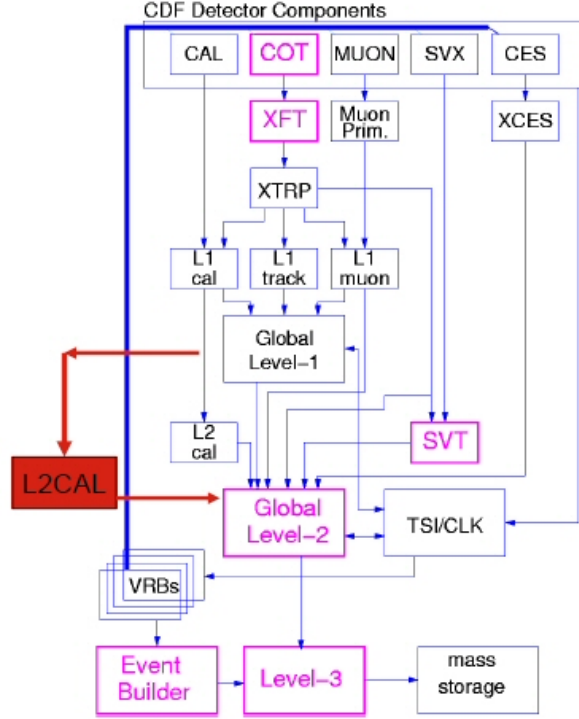
Figure 2.7: Diagram showing the upgraded trigger system in the CDF detector.

time the event is lost. L1 decision are made on average in about 4 μs : no dead time is expected from this level. Level 1 rejects 97% of the events, by reducing the event rates from 2.53 MHz to less than 40 kHz. The L1 decision is generated using information from:

- XFT (extremely fast tracker), which reconstructs approximate tracks ($p_T > 1.5$ GeV/c) in the transverse plane by exploiting information from COT superlayers. These tracks are extrapolated to the calorimeters and muon chambers to contribute to all trigger levels;

- the calorimeter towers, which carry information on the electromagnetic and hadronic energy deposits (*seeds*, which can initiate electron/photon or jet identification);

- the *muon stubs* (segment of tracks reconstructed in the muon chambers), which are matched to the XFT tracks.

LEVEL 2 is an asynchronous system which processes events that have received a L1 accept in a FIFO (First In, First Out) manner. It is structured

as a two stage pipeline with data buffering at the input of each stage. The first stage is based on dedicated hardware processors which assemble information from a particular section of the detector. The second stage consists of a computer which uses the list of objects generated by the first stage and implements in software the event selection. Each of the L2 stages is expected to take approximately 10 μs with a latency of approximately 20 μs . The input buffers can store up to four events. After the LEVEL 2 , the event rate is reduced to about 1 KHz (rejection factor ~ 40). The purposes of L2 are:

- to cluster the energy deposited in the towers around L1 seeds, as an approximate measure of electron, photon or jet energy;

- to use calorimeter and CES chamber information to improve separation of $e^{\pm}$ and γ from hadrons;

- to improve the matching between XFT tracks and muon stubs in order to have a better muon signature;

- to provide a measurement of the track impact parameters by means of the Silicon Vertex Trigger element (SVT), which allow to select events with secondary vertices from decay of long-lived heavy-flavour hadrons.

LEVEL 3 is a software trigger. It is operated on a cluster of ~ 300 processors which reconstruct the entire event with the same accuracy as in the off-line analysis. The final decision to accept an event is made on the basis of a list of observables indicating candidate events of physical interest (top quark production events, W/Z events, Drell-Yan events, ...). Events that satisfy the Level 3 trigger requirements are transferred onward to the Consumer Server/Data Logger (CSL) system for storage first on disk and later on tape. The average processing time per event in Level 3 is in the order of 1 s. The Level 3 leads to a further reduction in the output rate, with an accepted maximum of about 100 Hz.

Chapter 3

Physical Object Reconstruction

The CDF sub-detectors described in the previous chapter are used to identify the products of $p\bar{p}$ collisions. The unprocessed, or "raw", electrical signals generated by the sub-detectors are processed to form physical objects. First, high-level objects, such as vertices, tracks, or calorimeter clusters, are reconstructed. The reconstruction of charged particle tracks is particularly important in the identification and momentum measured of charged particles. Following the reconstruction of high-level objects, the objects are combined to identify physical objects, such as electrons, muons, jets, or neutrinos.

3.1 Lepton Reconstruction and Identification

Lepton reconstruction depends on the type of lepton and its direction inside the detector. Although this work focuses on a final state containing large $\not{E}_T$ and hadronic jets, lepton identification is still essential, since in order to ensure statistical independence with analyses containing a lepton in the final state, one of the requirements applied to the preselection sample is to reject events with a reconstructed lepton (*lepton veto*).

In the following, we briefly describe how leptons are identified at CDF ; in particular, the categories we use in this analysis are the Central Electrons, the Plug electrons and the Central Muons. The quantities used to identify lepton candidates are:

- the total transverse energy of the electron cluster in the electromagnetic calorimeter E_T;

- p_T, the track transverse momentum;

- the ratio of the total hadronic cluster energy to the EM energy $E_{\mathrm{had}}/E_{\mathrm{em}}$;

- the position of the track vertex along the z-axis, Z;

- the number of axial superlayers containing a signal, AS, and the number of hits per superlayer, hpAS;

- the number of stereo superlayers containing a signal, SS, and the number of hits per superlayer, hpSS;

- the distance between the PES centroid and the PEM centroid, ΔR_{plug};

- the track impact parameter with respect to the primary vertex d_0;

- the ratio of the energy collected in 5 layers over the energy collected in 9 layers of the PES, in the u and v orthogonal directions, $PES_5 x9_u$ and $PES_5 x9_v$;

- the track isolation ISO4, defined as the scalar sum of transverse energies of the tracks in a cone radius $\Delta R = \sqrt{(\Delta \eta)^2 + (\Delta \phi)^2} < 0.4$ around the lepton candidate track;

- The χ^2 resulting from the comparison of the PEM shower profile of the electron candidate with the profile of test beam electrons, using a (3×3) cluster size, $\chi^2 (3 \times 3)$

- the matching between the candidate muon track and a stub in the CMU/CMP/CMX.

3.1.1 Electrons

The CEM and PEM electromagnetic calorimeter sub-dectors are used to identify electrons. The selection depends on the sub-detector and is shown in Table 3.1. In addition, electron candidates in the central calorimeter must match a track in the COT . With fake rates at the order of a few %, the electron identification efficiency is 0.923 ± 0.001 (0.837 ± 0.003) for central (plug) electrons.

3.1.2 Muons

Muons are formed by matching stubs in the muon sub-detectors with a track. The selection for muons is shown in Table 3.2. A number of requirements are used to reduce the fake rate. An isolation requirement, described above, is applied. Events consistent with activity from cosmic rays are vetoed. The calorimeter energy is required to be consistent with the energy deposited by

Central Electrons	
E_T	≥ 20 GeV
p_T	≥ 10 GeV
$E_{\mathrm{had}}/E_{\mathrm{em}}$	$< 0.055 + (0.00045 \times E)$
$|Z|$	≤ 60 cm
AS, hpAS	$> 3, 5$
SS, hpSS	$> 2, 5$
ISO4 $/p_T$	< 0.1
Plug Electrons	
E_T	≥ 20 GeV
$E_{\mathrm{had}}/E_{\mathrm{em}}$	$< 0.055 + (0.00045 \times E)$
PES_5x9_u	≥ 0.65
PES_5x9_v	≥ 0.65
ISO4 $/p_T$	< 0.1
$\chi^2 (3 \times 3)$	< 10
ΔR_{plug}	< 3 cm

Table 3.1: Central and Plug electrons identification criteria.

a minimum ionizing particle. With fake rates at the order of a few %, the muon identification efficiency is 90.52±0.37 (92.75±0.47) for CMUP (CMX).

Central Muons	
p_T	≥ 20 GeV
E_{em}	< 2 GeV $+ \max(0, 0.0115 \times p - 100)$
E_{had}	< 6 GeV $+ \max(0, 0.028 \times p - 100)$
$E_{\mathrm{had}}/E_{\mathrm{em}}$	$< 0.055 + (0.00045 \times E)$
$|Z|$	≤ 60 cm
AS, hpAS	$> 3, 5$
SS, hpSS	$> 2, 5$
$|d_0|$ (with silicon hits)	< 0.02 cm
$|d_0|$ (with no silicon hits)	< 0.2 cm
ISO4 $/p_T$	< 0.1
ΔX(CMU) (if CMUP)	< 7 cm
ΔX(CMP) (if CMUP)	< 5 cm
ΔX(CMX) (if CMX)	< 6 cm

Table 3.2: Central muons identification criteria.

3.1.3   Fake leptons

A small fraction of jets pass the lepton selections, creating a background to this search. They are referred to as fake leptons. Modeling of fake leptons has been shown to be unreliable; therefore, this source of background is estimated from data samples enriched with jets. These samples are collected using trigger paths with lead jet E_T thresholds of 20 GeV, 50 GeV, 70 GeV, and 100 GeV. Jet-like objects passing a very loose lepton selection are taken as the jets that have a non-negligible probability for passing the lepton selection. The "fake rate" is taken as the fraction of these jets that pass the lepton selection. Note that the actual number of isolated, or "real", leptons must be subtracted from the number that pass the lepton selection. Similarly, the number of lepton objects passing the very loose selection must be removed. Thefefore, the fake rate for lepton category i is

$$f_i = \frac{N_i(full \quad electron) - \sum_{jEW} N_{ij}(full \quad electron)}{N_i(denominator) - \sum_{jEW} N_{ij}(denominator)} \qquad (3.1)$$

Using f_i , the fake lepton background predictions are $B_i = f_i \times N_i$ (Denominator Objects). Note that photons that interact with the detector's material and convert to an electron-positron pair are not considered fake leptons.

3.2   Missing Transverse Energy

The partons making up the colliding protons and antiprotons carry a fraction of the parent particle's momentum. The fraction of momentum in the longitudinal direction is unknown. On the other hand, the momentum in the transverse plane resulting from the Fermi motion inside the parent particle is known to be on the order of 0.1 GeV/c and is therefore negligible. Conservation of momentum requires that the total transverse momentum of the final state is zero. From a measured momentum imbalance in the transverse plane, known as missing transverse energy, one may infer that a particle may have escaped without detection.

Events with large missing transverse energy are selected in this analysis. A thorough and accurate reconstruction of this quantity is essential.

The x and y components of missing transverse energy are defined as

$$\not{E}_x = -\sum_i^{\text{towers}} {E_T}^i \cos\phi_i \qquad (3.2)$$

$$\not{E}_y = - \sum_{i}^{\text{towers}} {E_T}^i \sin \phi_i, \tag{3.3}$$

where the sum is taken over all towers that are above a threshold of 0.1 GeV , and the total electromagnetic and hadronic energy in the ith tower is E_T^i. The magnitude of the missing energy and its azimuthal direction are then calculated as

$$\not{E}_T = \sqrt{\not{E}_x^2 + \not{E}_y^2} \tag{3.4}$$

$$\phi(\not{E}_T) = \arctan \left(\frac{\not{E}_y}{\not{E}_x} \right) \tag{3.5}$$

3.2.1 Fake Missing Transverse Energy

In this search, missing transverse energy is used to identify the presence of invisible particles. However, there are several effects that may also lead to the experimental signature of $\not{E}_T$. These are:

- mismeasured energy resulting from problem with a calorimeter tower's electronics or calibrations;

- mismeasured energy resulting from uninstrumented calorimeter regions. In this case, the energy of a jet, for instance, is underestimated;

- Lost interaction prongs at very small angles;

- halos of muons, produced in collisions between the beam and gas or beam collimators, that travel parallel to the beam and cross rows of calorimeter towers along the z -axis. These produce energy deposits asymmetrically in ϕ ;

- minimum ionizing particles, such as muons, that travel through the calorimeter with only a small energy loss.;

- cosmic muons.

3.2.2 $\not{E}_T$ corrections

The $\not{E}_T$ measured by the CDF calorimeter (*raw $\not{E}_T$*) needs to be corrected for the same reasons that the jet energies do, as described in section 3.3. Hence, the $\not{E}_T$ needs to be recomputed using the corrected values of the jet

energies. The event $\not{E}_T$ is thus corrected using the corrected $E_T{}^{\text{corr}}$ values, according to the formulas

$$\not{E}_x{}^{\text{corr}} = \not{E}_x{}^{\text{raw}} + \sum_i^{\text{jets}} \left(E_x^{\text{corr},i} - E_x^{\text{raw},i} \right) \tag{3.6}$$

$$\not{E}_y{}^{\text{corr}} = \not{E}_y{}^{\text{raw}} + \sum_i^{\text{jets}} \left(E_y^{\text{corr},i} - E_y^{\text{raw},i} \right) \tag{3.7}$$

The azimuthal direction of the corrected $\not{E}_T$ is also corrected:

$$\phi(\not{E}_T{}^{\text{corr}}) = \arctan \left(\frac{\not{E}_y{}^{\text{corr}}}{\not{E}_x{}^{\text{corr}}} \right) \tag{3.8}$$

The $\not{E}_T$ energy used everywhere in this analysis is the corrected $\not{E}_T$.

3.3   Jet Reconstruction

Jets are collimated showers of hadrons produced in the hadronization of quarks and gluons. Jets produce large energy deposits in localized areas of the detector, and from these energy deposits the energy and direction of the originating parton can be inferred. To reconstruct jets, CDF developed several different reconstruction algorithms. We briefly describe the algorithm adopted in this work.

3.3.1   JETCLU algorithm

Jets are reconstructed using a cone algorithm known as JETCLU [33]. JET-CLU consists of three steps. First, adjacent calorimeter seed towers (those with $E_T > 1$ GeV) are clustered into preclusters. The maximum allowed size of a precluster in the η -ϕ plane is $2R_{\text{cone}} \times 2R_{\text{cone}}$, where R_{cone} is the clustering algorithm's size parameter.

Second, a cone is calculated for each precluster. A cone is defined from the seed towers of the precluster and all towers with $\Delta R = \sqrt{\Delta\eta^2 + \Delta\phi^2} < R_{\text{cone}}$ from the highest energy tower. An iterative procedure is then applied to refine the choice of included towers. The centroids of the cones are calculated. The identification of the members of the cones and the calculation of their centroids is repeated until the old centroids (the cone axes) agree with the new ones.

In a last step, overlapping stable cones have to be reconsidered because each calorimeter tower may only belong to one jet. A pair of overlapping cones

is merged if more than 75% of the transverse energy of one of the cones is shared by the other one. Otherwise they are separated using an iterative algorithm. The towers are redistributed to the cone whose centroid is closest and the centroids are recalculated until a stable configuration is reached.

The transverse energy and the position of the reconstructed jet are then given by:

$$E_T^{\text{jet}} = \sum_i E_T^i \tag{3.9}$$

$$\eta = \frac{1}{E_T^{\text{jet}}} \sum_i E_T^i \eta^i \tag{3.10}$$

$$\phi = \frac{1}{E_T^{\text{jet}}} \sum_i E_T^i \phi^i \tag{3.11}$$

where E_T^i, η_i and ϕ_i are the trasnverse energy and the position of the i-th tower.

Chapter 4

Event selection at CDF

The measurement of the $H \to$ invisible, produced in association with $Z \to \ell^+\ell^-$ cross section and the comparison with the best available Standard Model (SM) predictions is the main goal of the analysis described in this chapter. The full dataset collected from the CDF detector has been used for this analysis. In this Chapter is described how is collected the sample of data used to perform both the analysis and how the charged lepton events are reconstructed.

4.1 Lepton categories

Candidate leptons, once recorded, are separated into nine mutually exclusive categories: four for electrons; four for muons; and one for tracks that extrapolate outward to detector regions with insufficient calorimeter coverage for energy measurement. Such track-based candidates are required to satisfy the same quality requirements applied to the stubless muon candidates in the region $|\eta| \leq 1.2$. The electron categories are two central ones ($|\eta| < 1.1$), designated TCE and loose LCE, depending on the findings of the silicon-detector-based tracking algorithm, and two forward ones subject to the findings of the COT tracking algorithm ($1.2 < |\eta| < 2.0$), designated PHX (with phoenix track and charge information) and PEM (without the phoenix track and charge information). First two muon categories use the muon chambers (CMUP and CMX) and the other two use tracks matched with energy deposits consistent with minimum ionization in the central calorimeters for third muon category (CMIOCES) or forward calorimeters for third muon category (CMIOPES). Muon candidates of first category have left a characteristic stub in the muon chambers : central muon detectors ($|\eta| < 0.6$), central muon extension detectors ($0.6 < |\eta| < 1.0$), and the intermediate

muon detector ($1.0 <| \eta| < 1.5$). The experimental acceptance coverage of the respective electron and muon categories are shown on Figs. 4.1, 4.2
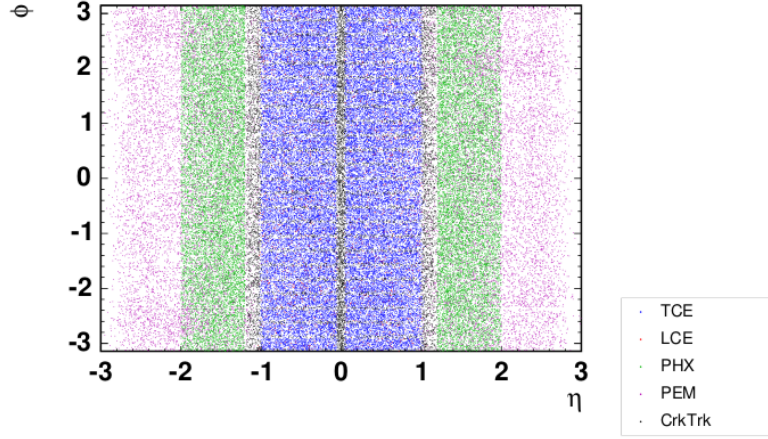
Figure 4.1: Acceptance coverage for different electron categories (TCE, LCE, PHX, PEM, CrkTrk) after the lepton trigger.
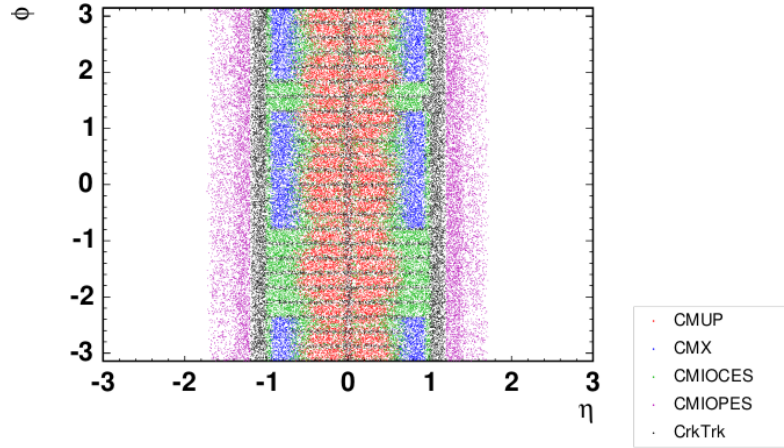
Figure 4.2: Acceptance coverage for different muon categories (CMUP, CMX, CMIOCES, CMIOPES, CrkTrk) after the muon trigger

To define these categories several cuts are applied to event parameters. Candidate selection for electrons selects on a ratio of HAD-to-EM energy consistent with an electromagnetic shower and is referred to as either central

or forward category, depending on whether the candidate is identified in the central or forward calorimeter. Central electron identification requires a high-quality charged particle in the COT with $P_T \geq 10$ GeV/c, that extrapolates to the central SMX detector and is matched to an EM energy cluster in the central calorimeter. A forward electron candidate is subject to the same conditions as the central one, except that it must be detected in the forward SMX detector and its track matched to the forward calorimeter. Both central and forward electron candidates are selected using a likelihood method to combine electron identification variables into a single discriminant. In order to reduce background from photons matched to misreconstructed calorimeter-seeded tracks, for each forward electron candidate we also require that its calorimeter-seeded track is consistent with a track reconstructed in the silicon detector only. Forward ($|\eta| \geq 1.2$) muon reconstruction requires strict constraints on the number of COT hits and the χ^2 of the track fit to suppress background from in-flight decays of pions and kaons. The point of the closest approach for the muon track is also required to be consistent with the $p\bar{p}$ interaction point to suppress the background from cosmic rays.
The cuts on detector quantities follow [32]:

- E_{HAD}/E_{EM} - the ratio of the hadronic calorimeter energy to the electromagnetic calorimeter energy associated with the candidate

- E_T/P_T - the ratio of the EM cluster transverse energy to the COT track transverse momentum

- Lshr - the lateral shower profile in the transverse plane to the electron direction

$$Lshr = 0.14 \frac{\sum_i M_i - P_i}{\sqrt{(0.14\sqrt{E_{EM}})^2 + \sum_i (\Delta P_i)^2}} \qquad (4.1)$$

where i is the sum over adjacent towers, M_i is the measured energy, and Pi is the predicted energy in the ith tower [32].

- $CalIso$ - The energy ET in a cone of radius $\Delta R = \sqrt{(\Delta\eta)^2 + (\Delta\phi)^2} \leq 0.4$ around the electron cluster excluding the electron cluster divided by the energy in the electron cluster

$$CalIso = \frac{E_T^{cone} - E_T^{electron}}{E_T^{electron}} \qquad (4.2)$$

- $TrkIso$ - the same variable as above $CalIso$ but measured using tracks instead of calorimeter

- $Q \times \delta x CES$ - The distance in the $r - \phi$ plane between the extrapolated, COT beam constrained track and the best matching CES cluster, times the charge Q of the track.

- $\Delta z CES$ - The distance in the $r - z$ plane between the extrapolated, COT beam constrained track and the best matching CES cluster.

- $NCotHitsAx$ - number of COT hits on axial layers belonging to track associated to thecandidate electron

- $NCotHitsSt$ - number of COT hits on stereo layers belonging to track associated to the candidate electron

- $\chi^2 COT$ - χ^2 associated with the COT hits belonging to track

- $NSvxHits$ - number of SVX hits belonging to track associated to the candidate electron

- $TrackP_T$ - Transverse momentum measured from the charged particle's track

- Track z_0 - Position along the longitudinal direction of the beamline.

- Track d_0 - Position along the transverse direction of the beamline.

- Axial and Stereo Superlayer - The number of axial and stereo super-layers in the COT having at least 5 hits associated to the track in question.

- $CES\Delta X$ - The difference in the $r - \phi$ plane between the best CES match and the COT beam-constrained track extrapolation to the CES.

- PEM 3x3 Fit - A χ^2 fit to electron test beam data of nine Plug EM towers.

- PES 5x9 U/V - The ratio of the central five tower energy to the total nine tower energy.

- χ^2 - This chi squared compares the fitted track to the actual hits in the trackers.

- Curvature Significance - The measured track curvature divided by the curvature error.

	TCE/LCE
Fiducial	CES
Track P_T	$>= 10(5$ if $E_T < 20)$
Track z_0	≤ 60cm
$NCotHitsAx$	≥ 3
$NCotHitsSt$	≥ 2
HAD/EM	≤ 0.05
Iso/E_T	0.1
TCE only	
Lshr	≤ 0.02
E_T/P_T	< 2.5
$CES\Delta X$	$-3 \leq q\Delta X \leq 1.5$ cm
$\Delta zCES$	< 3 cm

Table 4.1: Selection for central electrons.

	PHX/PEM
rapidity	$1.2 < \lvert\eta\rvert < 2$ (2.8 PEM)
HAD/EM	≤ 0.05
PEM 3x3 Fit	true
PES 5x9 U	≤ 0.65
PES 5x9 V	≤ 0.65
Iso/E_T	0.1
$\Delta R(PES, PEM)$	≤ 3.0
PHX only	
NHitsSi	≥ 3
Phenix match	true
Track $z0$	≤ 60cm
PEM	not above PHX requirements

Table 4.2: Selection for forward electrons with phoenix track and without the track

The definition of lepton categories regarding experimental cuts from above is shown in Tables. 4.1- 4.7

The $p\bar{p}$ interactions have high enough energy to tear the quarks of the proton and antiproton out of their hadronic configurations. When this happens, they will subsequently recombine or even create pairs out of the vacuum. This typically results in a spray of particles with a common general direction or "jets". As such, jets tend to deposit energy in both the EM and hadronic calorimeters assiciated with multiple tracks. In the analysis, jets are defined

	base muon cuts
P_T	> 10 GeV
E_{EM}	$2 + max(0, (P - 100) \cdot 0.0115)$
E_{HAD}	$6 + max(0, (P - 100) \cdot 0.028)$
$CalIso$	< 0.01
Axial SL	≥ 3
Stereo SL	≥ 2
Track z_0	≤ 60cm
Track d_0	$0.2cm$ (< 0.02 cm with silicon)
$\chi^2/d.o.f$	< 4.0

Table 4.3: Base muon cuts

	CMUP/CMX/CMU
CMU Fiducial	$x - fid < 0cm \quad z - fid < 0cm$
CMP Fiducial	$x - fid < 0cm \quad z - fid < -3cm$
CMX Fiducial	$x - fid < 0cm \quad z - fid < -3cm$
ΔX_{CMX}	< 6
ΔX_{CMU}	< 7
ΔX_{CMP}	< 5
CMX only	
COT Exit Radius	$> 140cm$
CMX Stub	true
Fiducial to CMX Arches	true
Fiducial to CMX Miniskirt	false
Fiducial to CMX Keystone	false
CMUP only	
CMU Stub	true
CMUP Stub	true
CMU only	
CMU Stub	true

Table 4.4: Selection for CMUP, CMU and CMX muons.

as calorimeter clusters within a cone of opening $\Delta R < 0.4$ in the ϕ, η space, with a total energy of $E_T > 15$ GeV. The number of jets in a particular event are an important variable for discriminating the WH and ZH signals from their backgrounds.

All lepton candidates are required to be isolated from its surroundings in such a way that the sum of the E_T for the calorimeter elements in a cone of $\Delta R < 0.4$ around each lepton is less than 10% of the E_T for electrons or 10%

	CMIOCES/CMIOPES
$E_{EM} + E_{HAD}$	> 0.1 GeV
veto	CMUP and CMX
CMIOCES only	
track fiducial	CES
Axial SL	≥ 3
Stereo SL	≥ 3
$\chi^2/d.o.f$	< 3.0
CMIOPES only	
track fiducial	PES
COT hit fraction	> 0.6

Table 4.5: Selection for CMIOCES and CMIOPES muons.

	BMU
BMU fiducial	true
BMU stub	true
PES fiducial	true
NSvxHits	≥ 3
CalIso	≥ 0.1 GeV
COT hits fraction	> 0.6
Curvature significance	> 12

Table 4.6: Selection for BMU muons.

of P_T for muons and extrapolated tracks. For lepton types in the central region where the tracking reconstruction allows it, a track-based isolation criterion is applied. This criterion requires there is no more than 10% of the electron E_T or muon P_T in other tracks within a cone of $\Delta R < 0.4$ around the lepton track. The Higgs boson candidates are selected from events with exactly two lepton candidates. At least one lepton is required to match level full electron category requirements and have $E_T > 20$ GeV ($P_T > 20$ GeV/c) for electrons (muons). This requirement is relaxed to 10 GeV/c for the extrapolated track category to increase the kinematic acceptance, particularly for lower m_H. A requirement is imposed for a dilepton invariant mass to cover $m_{ll} > 16$ GeV/c^2 to account to the fake leptonic signal from multijet events. The z-positions of the lepton candidates at the point of closest approach to the beam line are required to be within 4 cm of each other to reduce backgrounds from overlapping $p\bar{p}$ collisions. All of the category definitions are defined so as to be sensible above a P_T/E_T cut of 10 GeV, although they are only triggerable above 20 GeV.

	CrkTrk
Iso/P_T	≤ 0.1
Track z_0	$\leq 60cm$
Track d_0	$0.2cm$
$\chi^2/d.o.f$	< 3.0
Axial SL	≥ 3
Stereo SL	≥ 3
	not a CMX or CMUP veto
	not track PES or CES fiducial

Table 4.7: Selection for crack track leptons.

Because the CrkTrk can be either an electron or a muon, a difficulty arises in defining the calorimeter isolation variable. The standard calculation of isolation for muons excludes the towers into which the muon candidate projects, but for EM objects the isolation excludes all the towers in the EM cluster. In order to avoid an electron that could be identified as a CrkTrk from self vetoing, a related EM object for each candidate is searched for. It is required that the CrkTrk is isolated on the basis of the nearest EM object within $\Delta R < 0.05$. Finally when calculating E_T , the CrkTrk is treated as a muon, but the energy of the nearest EM cluster is removed if within $\Delta R < 0.05$.

4.1.1   Efficiency of lepton selection

In order to measure the efficiencies for lepton category trigger, we use Z candidates selected with one leg that has passed a full lepton selection (tag-leg) and one leg that is a base object for the lepton type (probe-leg). The probes are constructed out of the set of experimental requirements that are subset of the full lepton selection. We then measure the efficiency of the a complete selection (tight) which uses the probe as is base object. The tag and tight selection may or may not be the same. For example we use both as TCE to assess TCE efficiency, but we use TCE as the tag and PHX as the tight to assess the PHX efficiency. We can then write the efficiency of the tight selection as

$$\epsilon_{probe \to tight} = \frac{2N_{VV} + N_{VT}}{2N_{VV} + N_{VT} + N_{VF}} \tag{4.3}$$

Here V denotes "tagged", T "tight" and F "passed probe". The probe cuts for all the lepton categories are shown in [**?**].
We subtract the backgrounds using the Z peak sidebands. This is done for each for the $N_{VV}, N_{VT}, and N_{VF}$ by subtracting the yields in the Z sidebands

Central probe (TCE/LCE)
CES fiducial track $P_T > 5$ track $z_0 \leq 60cm$

PHX id probe
$1.2 < (PES)\eta < 2$ $E_{HAD}/E_{EM} \leq 0.05$ track match: true $NSiHits \geq 3$ track $z_0 \leq 60cm$

PHX tracking probe
$1.2 < (PES)\eta < 2$ $E_{HAD}/E_{EM} \leq 0.05$ $Iso/P_T \leq 0.1$ PEM3x3FitTower: true   PEM3x3$\chi^2 \leq 10$ $Pes5x9U \geq 0.65$ $Pes5x9V \geq 0.65$ $\Delta R(PES, PEM) \leq 3.0$

PEM probe
$1.2 < (PES)\eta < 2.8$ $E_{HAD}/E_{EM} \leq 0.125$

Table 4.8: Probes used for the electron efficiency calculation.

Central muon probe (CMUP/CMX/CMIOCES/CrkTrk)
PES fiducial: false   Axial SL ≥ 2 Stereo SL ≥ 2 track $z_0 \leq 60cm$

Forward muon probe (CMIOPES)
PES fiducial: true   COT hits fraction > 0.6 track $z_0 \leq 60cm$

Table 4.9: Probes used for the muon efficiency calculation.

(61 to 76 GeV and 106 to 121 GeV) from the Z peak (76 to 106 GeV) yields. This procedure works regardless of the leakage l of signal into the sideband as long as the efficiency does not depend on the mass. To see how this considers the the yield variables, the final yield sed in the Eq. 4.3 is

$$N_{VV} = (1 - l)N_{VV}^{sig} + N_{VV}^{bcgr} - (lN_{VV}^{sig} + N_{VV}^{bcgr}) \tag{4.4}$$

4.2 Online triggers

The events we consider must pass one of four online selections, triggers, before being recorded. Three complementary track pattern recognition algorithms have been used and are distinguished by their starting point: hits in the COT, hits in the silicon tracker, or the projections of observed calorimeter energy clusters back to the interaction region (calorimeter-seeded tracks). First online electron trigger requires an electromagnetic (EM) energy cluster in the central calorimeter ($|\eta| < 1.1$) with $E_T > 18$ GeV matched to a track found in the COT with $P_T > 8$ GeV/c. A second online electron trigger requires an EM energy cluster with $E_T > 20$ GeV in the forward ($1.2 < |\eta| < 2.0$) calorimeter and the missing transverse energy $\not{E}_T > 15$ GeV. The variable $\not{E}_T$, which indicates the presence of neutrinos, is defined as $\not{E}_T = |\sum_i E_i \hat{n}_{T,i}|$, where $\hat{n}_{T,i}$ is the transverse component of the unit vector pointing from the interaction point to the i-th tower of the calorimeter and E_i is the energy deposit in the i-th tower of the calorimeter. The E_T calculation is corrected for muons and track-based reconstructed leptons, which do not deposit all of their energy in the calorimeters. The transverse energy E_T is $E \sin \theta$, where E is the energy integrated over a calorimeter element or energy cluster. Similarly, P_T is the momentum component transverse to the beam line associated to the track of a particular particle. Muon triggers require the track segments in the several muon chambers to be matched to a COT track with $P_T > 18$ GeV/c. τ leptons are included only if they are detected indirectly through their decays to electrons or muons. Jets are reconstructed in the calorimeters using a cone algorithm (jetclu [37]) with a clustering radius of $\Delta R = (\Delta\eta)^2 + (\Delta\phi)^2 = 0.4$ and are corrected to the parton energy level using standard techniques [38]. Jets are selected if they have $E_T \geq 15$ GeV/c and $|\eta| < 2.4$.

Trigger efficiencies are measured using data from the leptonic W and Z decay. In order to preserve pairs of leptons in close proximity to one another, if an additional muon or electron candidate is found within the $\Delta R \leq 0.4$ cone, calorimeter towers associated with this lepton are not included in the overall E_T sum. An explicit requirement that the opening radius among all the reconstructed leptons is greater than 0.05 guarantees that any two different leptons are not based on the same track.

4.3 Event Selection

To measure the ZH cross section in the $\ell\ell + inv$ decay channel we apply a similar strategy to the one applied in the analysis done at CDF for $H \to$

$ZZ \rightarrow 4\ell$ [31]. We start selecting one $Z \rightarrow \ell\ell$ in the detector, then we try to get indirect information about $H \rightarrow inv$ from the unbalance in the detector transverse plane. The two undetected neutrinos should result in a significant $\not{E}_T$ in the final state. From the sample of events collected with the single high$-p_T$ triggers we select events containing exactly two isolated leptons, belonging to one of the lepton categories listed in Section 4.1. The leptons are required to have $p_T \geq 45$ GeV/c .

To reconstruct the $Z \rightarrow \ell\ell$ decay we require that the two leptons form a same favor and opposite charge pair $(e^+e^-, \mu^+\mu^-)$ with $76 \leq M_{ll} \leq 106$ GeV/c^2 . These requirements have only a marginal acceptance on $Z \rightarrow \tau\tau$ production which is included in this analysis only when both τs decay to e or μ satisfying the other kinematic requirements.

These requirements define a preselected sample of dilepton events dominated by the single Z production $(Drell - Yan)$ which is predicted to be produced with a cross section of $\sigma \approx 490pb$ for m$(\ell\ell) \geq 20$ GeV/c^2 at NNLo.

The main difference between $ZH \rightarrow \ell\ell + inv$ signal and the $Drell - Yan$ background are the two additionally produced particles in the final state. While in ZH production these should appear as a significant $\not{E}_T$ in the detector, the $Drell - Yan$ background can present (even large) due to instrumental effect. In order to eliminate the Drell-Yan background we require to have a $\not{E}_T \geq 60$ GeV.

These requirements define a preselected sample of dilepton events dominated by the $ZZ \rightarrow \ell\ell + inv$.

The main difference between $ZH \rightarrow \ell\ell + inv$ signal and the $ZZ \rightarrow \ell\ell + inv$ background is the kinematic of the decaying leptons. In the preselected sample we have additional contribution also from other diboson processes, $WW \rightarrow \ell\nu\ell\nu$ and $WZ \rightarrow \ell\nu\ell'\ell'$, that has both similar leptonic decay modes. An additional small contribution comes from $W\gamma$ and W+jets production, where a photon or a jet can mimic the second lepton in the final state. At last, $t\bar{t}$ production can give a dileptonic signature (when $t\bar{t} \rightarrow (W \rightarrow \ell\nu)\, b\, (W \rightarrow \ell\nu)b$) associated with a large hadronic activity in the calorimeters.

We model the kinematic of the ZH signal and of the several background processes using Monte Carlo (MC) simulations. The generator used, the predicted theoretical cross section, and the names of the dataset used in this analysis are well explained in the CDF analysis of ZZ decay in 4ℓ and $2\ell\,\nu\nu$ [39]. In this analysis the MC samples are normalized so as to reproduce the expected number of events in the considered integrated luminosity. The normalization of the $Drell - Yan$ simulated sample will be extracted from a fit to the data in a control sample kinematically similar to the one considered for the measurement.

The contribution from W+jets production with the misidentified jet mim-

icking one of the two leptons is evaluated from a sample of jet−triggered data with the fake rate method. In this case we consider only events with one real lepton and the possible fake second lepton. The events containing one real lepton and two candidate fake leptons are splitted and two lepton+fake candidate events are considered. Each candidate is weighted with the appropriate fake rate and added to the background prediction. Particular attention is given to the reconstructed $Z \to \ell\ell$ properties, i.e. the two lepton transverse momenta, the opening angles between the two leptons ($\Delta\phi(ll)$, $\Delta R(ll)$), the reconstructed Z mass (M_{ll}) and transverse momentum of the dilepton system ($p_T{}^Z$). In addition we check the modeling of some other global variables (N_{jets}, $\not{E}_T$) for these events. The data−to−MC comparison shows some disagreement that are due to intrinsic problems in the Drell−Yan MC simulation. These will not have a dramatic effect on the analysis since we will try to reduce the contribution from this process cutting on $\not{E}_T$. The Drell−Yan contribution in the final signal region will be extracted from a fit to the data in an orthogonal control region; the uncertainty extracted from the fit will be included as systematic uncertainty considered for the cross section measurement. In order to extract the $ZH \to \ell\ell + inv$ signal from the background dominated sample we exploit some kinematic properties of the reconstructed event. At first, since we don't expect $\ell\ell + inv$ events to have a large hadronic activity, we apply a veto on the presence of a Z−recoiling jet: we practically reject events that have any jet ($E_T \geq 15 GeV$, L5 corr.) with $\Delta\phi(j, Z) \geq \frac{\pi}{2}$. In the Drell−Yan background events (as well as W+jets) is often present a $high - E_T$ jet recoiling against the $Z \to \ell\ell$, hence this veto reduces this contribution while doesn't affect significantly the ZH signal. The veto applied select a sample composed for its $\approx 98\%$ by events with no reconstructed jet at all, still dominated by Drell−Yan events. To reduce the background and isolate ZH events we exploit indirect information on the additional Z decaying to a pair of neutrinos. In $ZH \to \ell\ell + inv$ signal we expect to observe a significant amount of $\not{E}_T$ due to the two undetected neutrinos, while single produced Z events should eventually present $\not{E}_T$ due mainly to detector resolution and instrumental effects. To further improve the signal-to-background ratio in the considered data sample and prevent from detector resolution mismodeling effects we require that the observed $\not{E}_T$ is

$$MET \geq 60 \, GeV \qquad (4.5)$$

In summary in order to study this process events are collected using $high-p_T$ muon, $high-E_T$ electron and Met+Pem triggers, using a dataset corresponding to 9.7 fb^{-1} of CDF data.

Chapter 5

Signal and Background modeling

We model the kinematic of the ZH signal and of the several background processes using Monte Carlo (MC) simulations. The generator used, the predicted theoretical cross section, and the names of the dataset can be viewed. In this analysis the MC samples are normalized so as to reproduce the expected number of events in the considered integrated luminosity. The normalization of the $Drell-Yan$ simulated sample will be extracted from a fit to the data in a control sample kinematically similar to the one considered for the measurement.

5.1 Signal Region

We define a Signal Region for this measurement selecting events passing the following requirements:
In order to reconstruct the $Z \to \ell\ell$ event the following features are requested:

- Exactly two Same Flavor and opposite Charge leptons

- Reconstructed invariant mass: $82 \leq M_{ll} \leq 100 \text{ GeV}/c^2$

- Different reconstructed lepton categories for electrons, muons and high$-$quality tracks

Events are required to be boosted in order to account of the recoil against the Higgs boson:

- Consider as a signal region $p_T(ll) \geq 45$ GeV

- $30 \leq p_T(ll) \leq 45$ GeV events considered as a control sample

In order to reduce spurious background boosted events that have $\not{E}_T$ and level 5 correction:

- No jets reconstructed that have $E_T \geq 15$ GeV and L5 corrections, with $\Delta\phi \geq 2.0$ from the Z

Events $ZH \rightarrow \ell\ell + inv$ are searched in the tail of the $\not{E}_T$ distribution Features ($\epsilon_{ID}, \epsilon_{trig}$, etc) and tools from ZZ cross section measurement and $H \rightarrow WW$ search.

Tables show the event selection for each sample during each stage of the analysis after the skim. We only present efficiencies for the signal region event selection.

	Z+jets		
Description	$Z \to e^+e^-$	$Z \to \mu^+\mu^-$	$Z \to \tau^+\tau^-$
Events after skim	434739	709579	12025
Cut 1 (dileptonType $\neq$ -1)	1	1	1
Cut 2 (dileptonFlavor $\neq$ kflav_ em | kflav_ etau | | kflav_ mtau)	0.99	0.99	0.58
Cut 3 (dileptonType $\neq$ k_ PHX_ PHX | | k_ PHX_ PLBE | | k_ PLBE_ PLBE)	0.99	0.98	0.96
Cut 4 (N_{jeAw} <0.)	0.78	0.79	0.82
Cut 5 ($\Delta\phi(\not{E}_T,ll) > 0.5$)	0.67	0.63	0.35
Cut 6 ($Z_{Pt} > 45.$ GeV/c)	0.0005	0.0005	0.0002
Cut 7 (82. <dimass < 100. GeV/c^2)	0.73	0.78	0.08
Cut 8 ($\not{E}_T > 60.$ GeV)	0.02	0.02	0
Cut 9 (cutMask == true)	1	0.95	nan
Cut 10 (SS regions reject PHX)	1	1	nan
Cut 11 (SS regions reject PHX)	1	1	nan
Overall efficiency	$3.36 \cdot 10^{-6}$	$3.18 \cdot 10^{-6}$	
Expected events	1.90	2.25	0.03

Description	W+jets
Events after skim	50331.9
Cut 1 (dileptonType $\neq$ -1)	0.90
Cut 2 (dileptonFlavor $\neq$ kflav_ em | kflav_ etau | | kflav_ mtau)	0.94
Cut 3 (dileptonType $\neq$ k_ PHX_ PHX | | k_ PHX_ PLBE | | k_ PLBE_ PLBE)	0.92
Cut 4 (N_{jeAw} <0.)	0.72
Cut 5 ($\Delta\phi(\not{E}_T,ll) > 0.5$)	0.60
Cut 6 ($Z_{Pt} > 45.$ GeV/c)	0.02
Cut 7 (82. <dimass < 100. GeV/c^2)	0.10
Cut 8 ($\not{E}_T > 60.$ GeV)	0.33
Cut 9 (cutMask == true)	0.31
Cut 10 (SS regions reject PHX)	1
Cut 11 (SS regions reject PHX)	1
Overall efficiency	$7.56 \cdot 10^{-5}$
Expected events	3.8 ± 0.6

|	$W\gamma$		
Description	$W \to e + \nu$	$W \to \mu + \nu$	$W \to \tau + \nu$
Events after skim	1041.1	695.81	65.86
Cut 1 (dileptonType $\neq$ -1)	1	1	1
Cut 2 (dileptonFlavor $\neq$ kflav_ em | kflav_ etau | | kflav_ mtau)	0.99	0.14	0.60
Cut 3 (dileptonType $\neq$ k_ PHX_ PHX | | k_ PHX_ PLBE | | k_ PLBE_ PLBE)	0.75	0.99	0.85
Cut 4 (N_{jeAw} <0.)	0.85	0.85	0.82
Cut 5 ($\Delta\phi(\not{E}_T,ll) > 0.5$)	0.92	0.93	0.86
Cut 6 ($Z_{Pt} > 45.$ GeV/c)	0.11	0.12	0.10
Cut 7 (82. <dimass < 100. GeV/c^2)	0.07	0.08	0.11
Cut 8 ($\not{E}_T > 60.$ GeV)	0.18	0.26	0.35
Cut 9 (cutMask == true)	0.30	0.67	0.68
Cut 10 (SS regions reject PHX)	1	1	1
Cut 11 (SS regions reject PHX)	1	1	1
Overall efficiency	$2.68 \cdot 10^{-4}$	$1.84 \cdot 10^{-4}$	$9.38 \cdot 10^{-4}$
Expected events	0.28 ± 0.01	0.13 ± 0.02	0.06
Tot. Expected Events	0.5 ± 0.1		

Description	$t\bar{t}$
Events after skim	1250.12
Cut 1 (dileptonType $\neq$ -1)	1
Cut 2 (dileptonFlavor $\neq$ kflav_ em | kflav_ etau | | kflav_ mtau)	0.61
Cut 3 (dileptonType $\neq$ k_ PHX_ PHX | | k_ PHX_ PLBE | | k_ PLBE_ PLBE)	0.98
Cut 4 (N_{jeAw} <0.)	0.17
Cut 5 ($\Delta\phi(\not{E}_T,ll) > 0.5$)	0.81
Cut 6 ($Z_{Pt} > 45.$ GeV/c)	0.52
Cut 7 (82. <dimass < 100. GeV/c^2)	0.12
Cut 8 ($\not{E}_T > 60.$ GeV)	0.87
Cut 9 (cutMask == true)	0.97
Cut 10 (SS regions reject PHX)	1
Cut 11 (SS regions reject PHX)	1
Overall efficiency	$4.36 \cdot 10^{-3}$
Expected events	5.5 ± 0.9

Description	WZ
Events after skim	733.75
Cut 1 (dileptonType $\neq$ -1)	0.99
Cut 2 (dileptonFlavor $\neq$ kflav_ em | kflav_ etau | | kflav_ mtau)	0.90
Cut 3 (dileptonType $\neq$ k_ PHX_ PHX | | k_ PHX_ PLBE | | k_ PLBE_ PLBE)	0.97
Cut 4 (N_{jeAw} <0.)	0.31
Cut 5 ($\Delta\phi(\not{E}_T,ll) > 0.5$)	0.77
Cut 6 ($Z_{Pt} > 45.$ GeV/c)	0.43
Cut 7 (82. <dimass < 100. GeV/c^2)	0.44
Cut 8 ($\not{E}_T > 60.$ GeV)	0.58
Cut 9 (cutMask == true)	0.83
Cut 10 (SS regions reject PHX)	1
Cut 11 (SS regions reject PHX)	1
Overall efficiency	$1.86 \cdot 10^{-2}$
Expected events	13.7 ± 1.5

Description	WW
Events after skim	1969.84
Cut 1 (dileptonType $\neq$ -1)	1
Cut 2 (dileptonFlavor $\neq$ kflav_ em | kflav_ etau | | kflav_ mtau)	0.60
Cut 3 (dileptonType $\neq$ k_ PHX_ PHX | | k_ PHX_ PLBE | | k_ PLBE_ PLBE)	0.97
Cut 4 (N_{jeAw} <0.)	0.83
Cut 5 ($\Delta\phi(\not{E}_T,ll) > 0.5$)	0.90
Cut 6 ($Z_{Pt} > 45.$ GeV/c)	0.41
Cut 7 (82. <dimass < 100. GeV/c^2)	0.11
Cut 8 ($\not{E}_T > 60.$ GeV)	0.52
Cut 9 (cutMask == true)	0.96
Cut 10 (SS regions reject PHX)	1
Cut 11 (SS regions reject PHX)	1
Overall efficiency	$9.76 \cdot 10^{-3}$
Expected events	19.2 ± 1.8

Description	ZZ
Events after skim	569.26
Cut 1 (dileptonType $\neq$ -1)	0.99
Cut 2 (dileptonFlavor $\neq$ kflav_ em | kflav_ etau | | kflav_ mtau)	0.97
Cut 3 (dileptonType $\neq$ k_ PHX_ PHX | | k_ PHX_ PLBE | | k_ PLBE_ PLBE)	0.98
Cut 4 (N_{jeAw} <0.)	0.27
Cut 5 ($\Delta\phi(\not{E}_T,ll) > 0.5$)	0.77
Cut 6 ($Z_{Pt} > 45.$ GeV/c)	0.46
Cut 7 (82. <dimass < 100. GeV/c^2)	0.75
Cut 8 ($\not{E}_T > 60.$ GeV)	0.71
Cut 9 (cutMask == true)	0.96
Cut 10 (SS regions reject PHX)	1
Cut 11 (SS regions reject PHX)	1
Overall efficiency	$4.77 \cdot 10^{-2}$
Expected events	27.2 ± 2.9

Description	$ZH\ m_H = 125$ GeV/c^2
Events after skim	20.60
Cut 1 (dileptonType $\neq$ -1)	1
Cut 2 (dileptonFlavor $\neq$ kflav_ em | kflav_ etau | | kflav_ mtau)	0.99
Cut 3 (dileptonType $\neq$ k_ PHX_ PHX | | k_ PHX_ PLBE | | k_ PLBE_ PLBE)	0.98
Cut 4 (N_{jeAw} <0.)	0.85
Cut 5 ($\Delta\phi(\not{E}_T,ll) > 0.5$)	0.91
Cut 6 ($Z_{Pt} > 45.$ GeV/c)	0.75
Cut 7 (82. <dimass < 100. GeV/c^2)	0.85
Cut 8 ($\not{E}_T > 60.$ GeV)	0.85
Cut 9 (cutMask == true)	0.96
Cut 10 (SS regions reject PHX)	1
Cut 11 (SS regions reject PHX)	1
Overall efficiency	0.40
Expected events	8.17

Description	Data
Events after skim	$1.42 \cdot 10^6$
Cut 1 (dileptonType $\neq$ -1)	0.97
Cut 2 (dileptonFlavor $\neq$ kflav_ em | kflav_ etau | | kflav_ mtau)	0.99
Cut 3 (dileptonType $\neq$ k_ PHX_ PHX | | k_ PHX_ PLBE | | k_ PLBE_ PLBE)	0.95
Cut 4 (N_{jeAw} <0.)	0.80
Cut 5 ($\Delta\phi(\not{E}_T,ll) > 0.5$)	0.64
Cut 6 ($Z_{Pt} > 45.$ GeV/c)	0.003
Cut 7 (82. <dimass < 100. GeV/c^2)	0.34
Cut 8 ($\not{E}_T > 60.$ GeV)	0.16
Cut 9 (cutMask == true)	0.78
Cut 10 (SS regions reject PHX)	1
Cut 11 (SS regions reject PHX)	1
Overall efficiency	$5.49 \cdot 10^{-5}$
Expected events	78

Given the mismodeling in Drell−Yan reproduction observed in the dilepton inclusive sample we extract the normalization of this process from an $e - \mu$ orthogonal sample with the kinematic properties similar to the SR considered. To reach a better agreement between data and MonteCarlo simulation
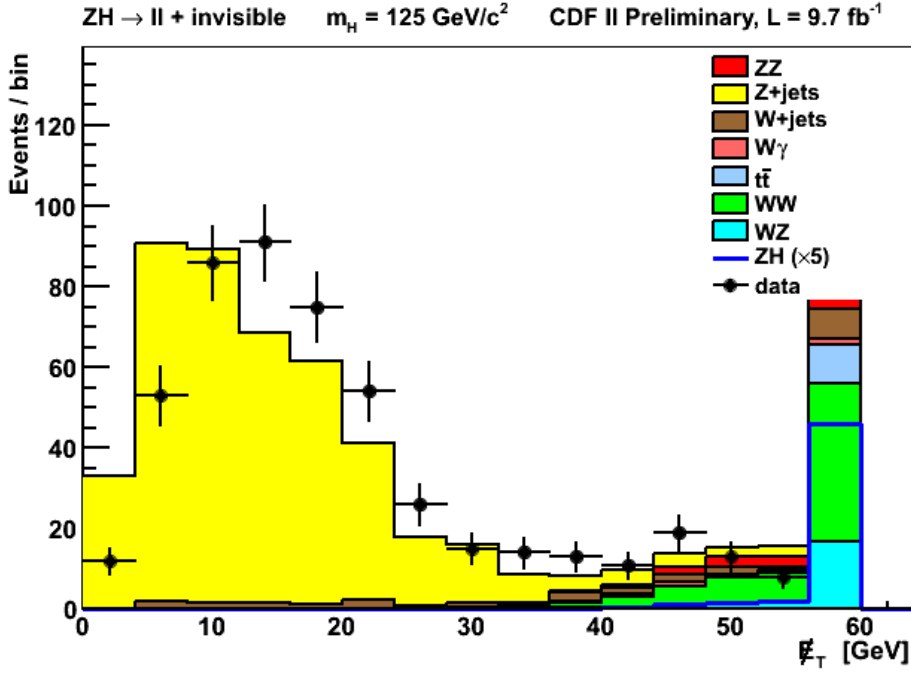
we shifted the $\not{E}_T$ distribution in the Signal Region by a factor of $+3 \pm 33\%$ GeV.

We fit the normalization of the Drell−Yan component from the $\not{E}_T \leq 60 GeV$ distribution of the data in the Signal Region, as a scale factor with respect to the nominal MC normalization, and apply the same one to scale the Drell−Yan contribution in the SR. The fit result in a correction factor

$$k = 1.7 \pm 0.5\% \ \times \ the \ nominal \ MC \ normalization \tag{5.1}$$

Table [5.1] shows the expected and observed number of events in the Signal Region in the full CDF dataset considered ($L = 9.7 \text{fb}^{-1}$) where we can see that the sample is dominated by ZZ, and WW contributions, with significant WZ and Drell-Yan signal contributions.

Figures [5.1] show the comparison between data and MC for the kinematic variables distribution that charachterize the events in the Signal Region.
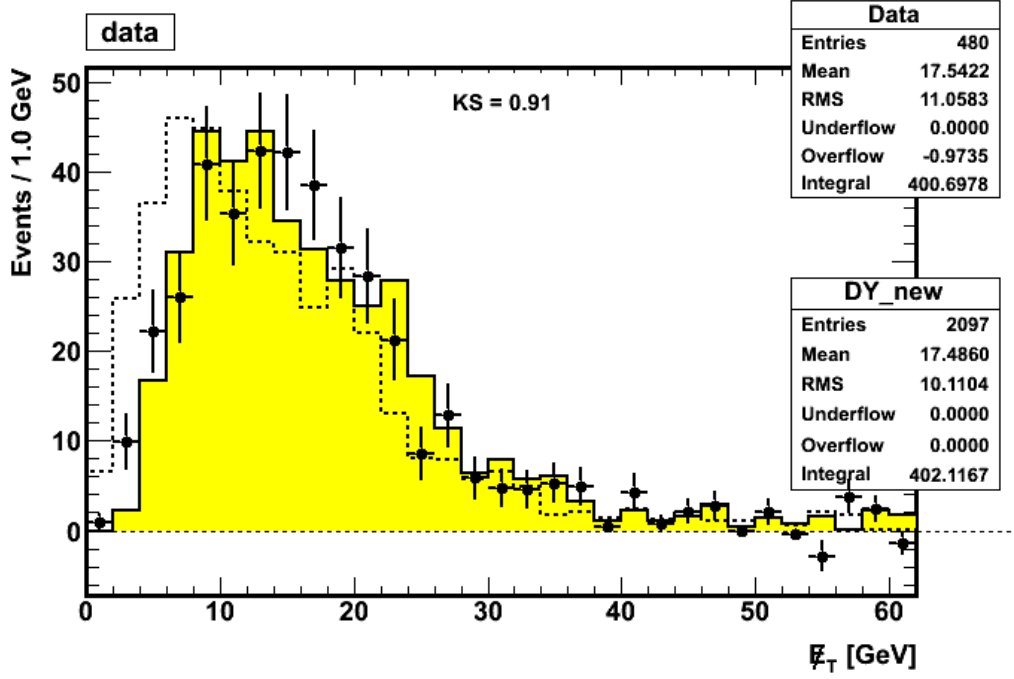
Table 5.1: Number of predicted and observed events in the Signal Region defined by no recoiling jets, $82 \leq M_{ll} \leq 100 GeV/c^2$, $\Delta\phi(MET, l) \geq 2.0$, $\not\!\!E_T \geq 60 GeV$

$ZH \rightarrow \ell^+\ell^- +$ **invisible** (signal region)	
CDF Run II Preliminary, $\mathcal{L} = 9.7$ fb^{-1}	
Z +jets	7.1 ± 3.1
$W+$ jets	3.8 ± 0.6
$W\gamma$	0.5 ± 0.1
$t\bar{t}$	5.5 ± 0.9
WZ	13.7 ± 1.5
WW	19.2 ± 1.8
ZZ	27.2 ± 2.9
Total prediction	76.9 ± 7.2
ZH ($m_H = 125$ GeV/c^2)	8.2 ± 1.3
Data	78

The expected contribution for the signal and background processes are obtained using the MC simulation described in Table [5.1] and the data−driven method for the W+jets contribution.

(a) $\Delta R(ll)$ between leptons

(b) $\Delta\phi(ll)$ between leptons

(c) Missing Transverse Energy

(d) $\Delta\phi$ between $\not{E}_T$ and leading lepton

(e) Transverse momentum of leading lepton

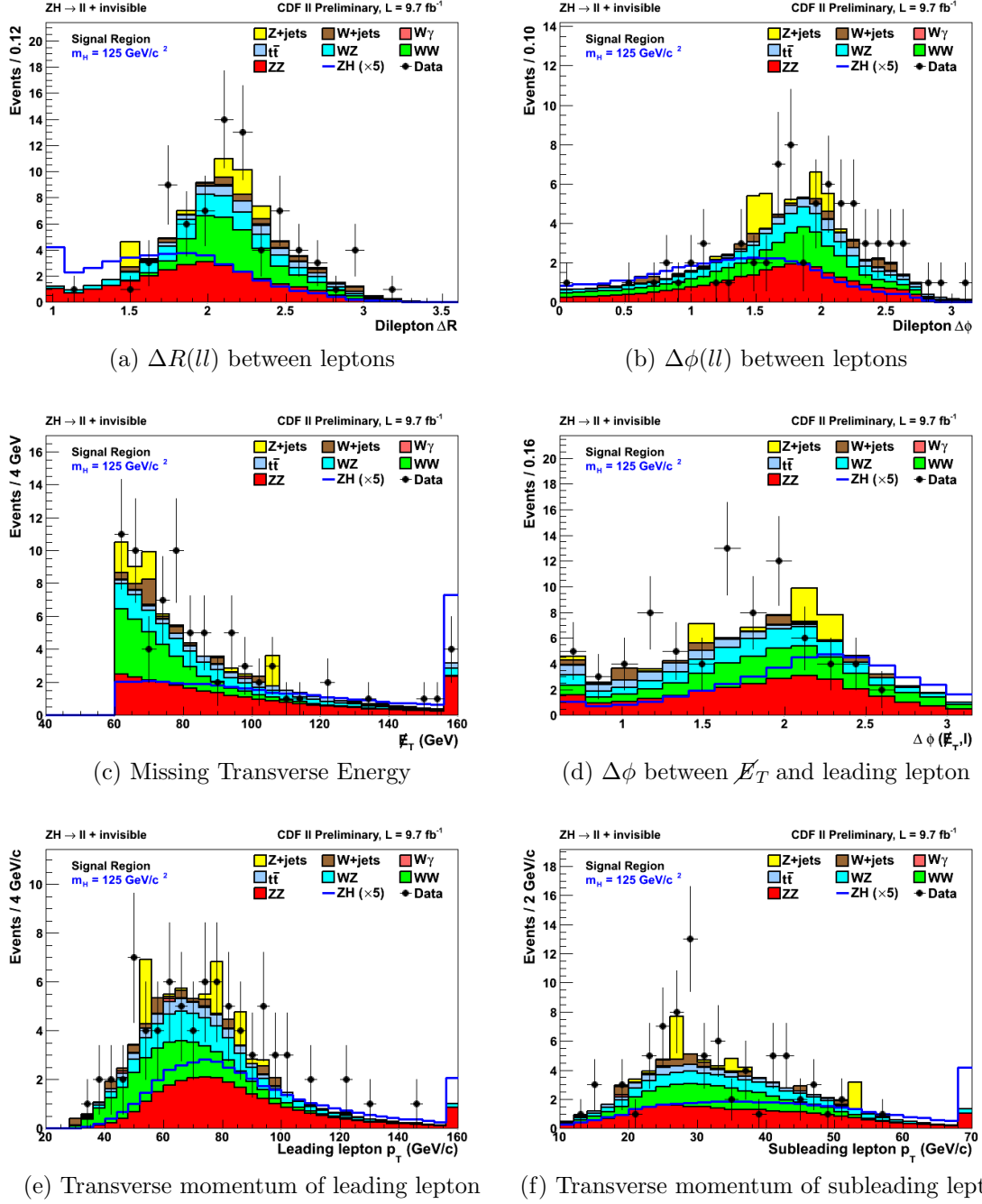(f) Transverse momentum of subleading lepton

Figure 5.1: Signal region

5.2 Background Modeling

The dominant background contributions in the previously defined Signal Region are due to ZZ and WW, which present similar signature in the final state but higher production cross section than ZH. WW production is kinematically similar to the ZZ diboson one, hence we would like to be able to model it fairly, exploiting a full Next-to-Leading order simulation. Drell-Yan residual contribution is mainly characterized by the presence of $\not{E}_T$ which doesn't reflect the production of undetected particles, mostly due to detector resolution effect, which is not trivial to model in the MC simulation. These background processes are tested in non-overlapping data sample of events:

- $e - \mu$ sample

- Same Sign sample

- Side Bands sample

5.2.1 $e - \mu$ Control Region

To test the WW modeling in a kinematic region similar to the Signal Region we select events with two isolated leptons in the final state of different flavor, i.e. $e^{\pm}, \mu^{\mp}$, satysfing all the requirements that define the Signal Region, but a different dilepton invariant mass range. Selecting different flavor leptons we drastically reduce contribution from real Z. A residual contribution of Drell-Yan events come from $Z \to \tau\tau$ decays with subsequent leptonic decays of the τs that can produce an $e - \mu$ pair. Since in this case the two leptons don't necessarily come from a Z we broaden the range of the considered dilepton mass spectrum, to increase the statistic of the control sample and modify the Signal Region requirement as follow:

- $40 \leq M_{e\mu} \leq 140 GeV/c^2$

This CR is used also to evaluate from data the proper normalization of the Drell-Yan background contribution in a kinematic region with large $\not{E}_T$, hence similar to the Signal Region. We do that considering the ΔR kinematic distribution and comparing simulation for the several processes to data. Fitting the Drell-Yan component to data in this control sample we obtain a correction k= $1.7 \pm 0.5x$ the MC nominal normalization.

This correction factor applied to the Drell-Yan simulation improve significantly the agreement between data and simulation in this CR and is applied

Table 5.2: Number of predicted and observed events in the $e\mu$ Control Region defined by an $e^{\pm}\mu^{\mp}$ pair, no jet with $E_T \geq 15\,GeV$ with $\Delta\phi(Z,J) \geq 2.0$ rad, $40 \leq M_{ll} \leq 140 GeV/c^2$, $\Delta\phi(MET,l) \geq 0.5$ rad, $\not{E}_T \geq 60 GeV$

$ZH \to \ell^+\ell^-$ + invisible ($e^{\pm}\mu^{\mp}$ control region)	
CDF Run II Preliminary, $\mathcal{L} = 9.7$ fb^{-1}	
Z +jets	9.3 ± 4.1
$W+$ jets	24.2 ± 3.6
$W\gamma$	16.9 ± 2.8
$t\bar{t}$	14.2 ± 2.3
WZ	2.4 ± 0.3
WW	96.4 ± 8.9
ZZ	0.17 ± 0.02
Total prediction	163.7 ± 12.6
Data	155

also to obtain the proper normalization for the Drell-Yan contribution in the Signal Region.

Table [5.2] summarizes the number of events expected from the several processes and the yields in the collected data. The most relevant kinematic variable distributions of the events in the $e - \mu$ Control Region for data and Monte Carlo are shown in Figures [5.2].

No significant discrepancy is noticeable in the data-to-simulation comparison, with uncertainties dominated by the limited statistics of the sample considered. once tested in this sample, we can assume that the simulation properly models the WW background also in the Signal Region.

(a) $\Delta R(ll)$ between leptons

(b) $\Delta\phi(ll)$ between leptons

(c) Missing Transverse Energy

(d) $\Delta\phi$ between $\not{E}_T$ and leading lepton

(e) Transverse momentum of leading lepton
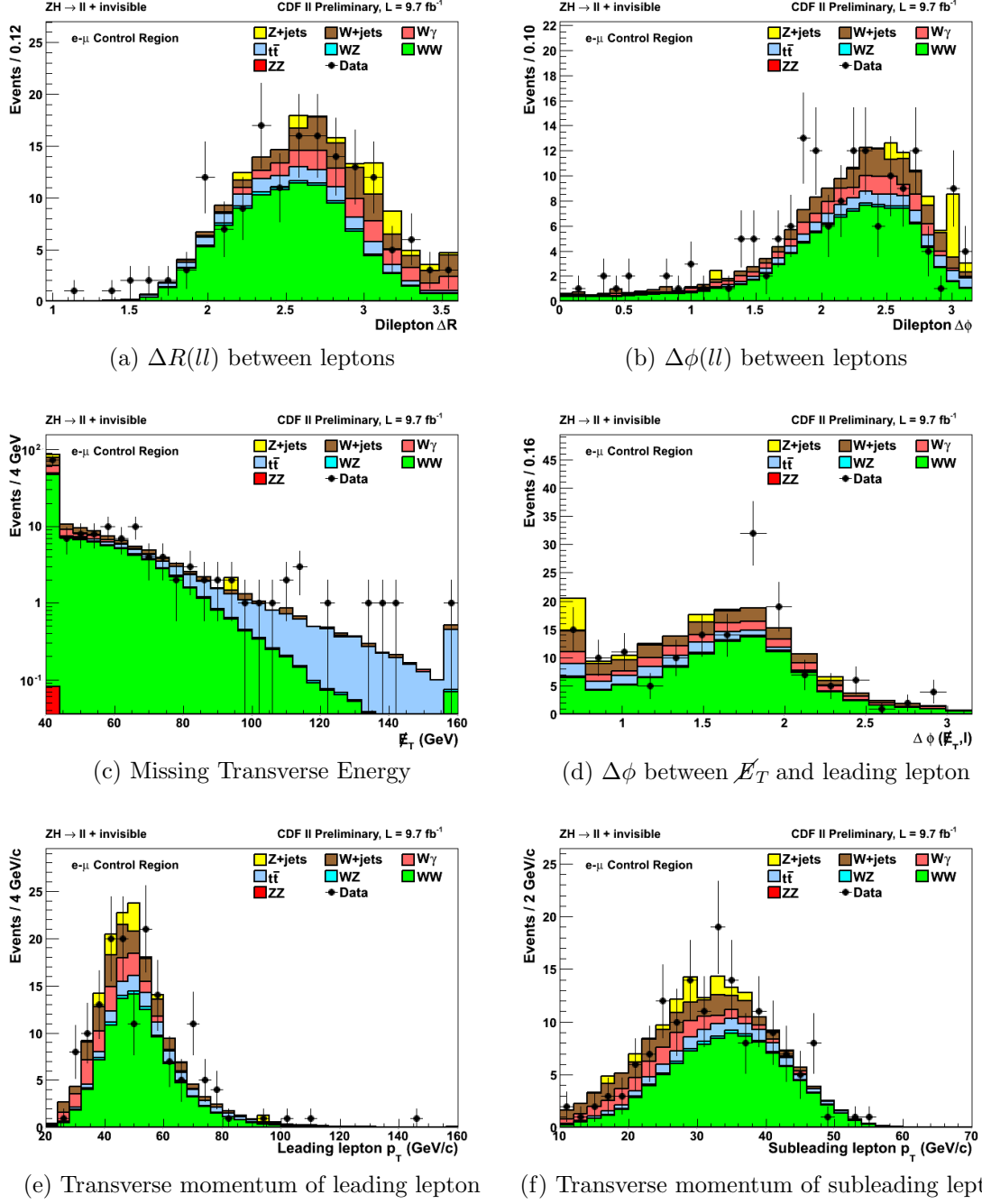
(f) Transverse momentum of subleading lepton

Figure 5.2: Opposite-flavor, opposite-sign control region

5.2.2 Same Sign Control Region

To test the W+jets modeling in a kinematic region similar to the Signal Region we select events with two isolated leptons in the final state of same sign, i.e. $e^{\pm}e^{\pm}, \mu^{\pm}\mu^{\pm}$, satysfing all the requirements that define the Signal Region, but a broader dilepton invariant mass range. Selecting same flavor leptons we drastically reduce contribution from real Z. Since in this case the two leptons don't necessarily come from a Z we broaden the range of the considered dilepton mass spectrum, to increase the statistic of the control sample and modify the Signal Region requirements as follow:

- Same Charge and Same Flavor lepton pair

- $40 \le M_{ll} \le 140 GeV/c^2$

- $\not{E}_T \ge 60$ GeV

- No jet with $E_T \ge 15 GeV$ (L5 corrections) with $\Delta\phi(Z, j) \ge 2.0 rad$

- $\min\Delta\phi(\not{E}_T, l) \ge 0.5$ rad

Table 5.3: Number of predicted and observed events in the Same-sign Control Region defined by a $l^{\pm}l^{\pm}$ pair, no jet with $E_T \ge 15 GeV$ with $\Delta\phi(Z, J) \ge 2.0$ rad, $40 \le M_{ll} \le 140 GeV/c^2$, $\Delta\phi(MET, l) \ge 0.5$ rad, $\not{E}_T \ge 60 GeV$

$ZH \to \ell^+\ell^- +$ **invisible** (same-sign control region) CDF Run II Preliminary, $\mathcal{L} = 9.7$ fb^{-1}	
Z +jets	2.9 ± 1.3
$W + jets$	30.1 ± 4.5
$W\gamma$	8.4 ± 1.4
$t\bar{t}$	0.22 ± 0.04
WZ	7.2 ± 0.8
WW	1.7 ± 0.2
ZZ	0.66 ± 0.07
Total prediction	51.1 ± 5.1
Data	57

Table [5.3] summarizes the number of events expected from the several processes and the yields in the collected data. The most relevant kinematic variable distributions of the events in the Same sign Control Region for data and Monte Carlo are shown in Figures [5.3]. No significant discrepancy is noticeable in the data-to-simulation comparison, with uncertainties dominated

by the limited statistics of the sample considered. Once tested in this sample, we can assume that the simulation properly models the W+jets background also in the Signal Region.

(a) $\Delta R(ll)$ between leptons

(b) $\Delta\phi(ll)$ between leptons

(c) Missing Transverse Energy

(d) $\Delta\phi$ between $\not{E}_T$ and leading lepton

(e) Transverse momentum of leading lepton
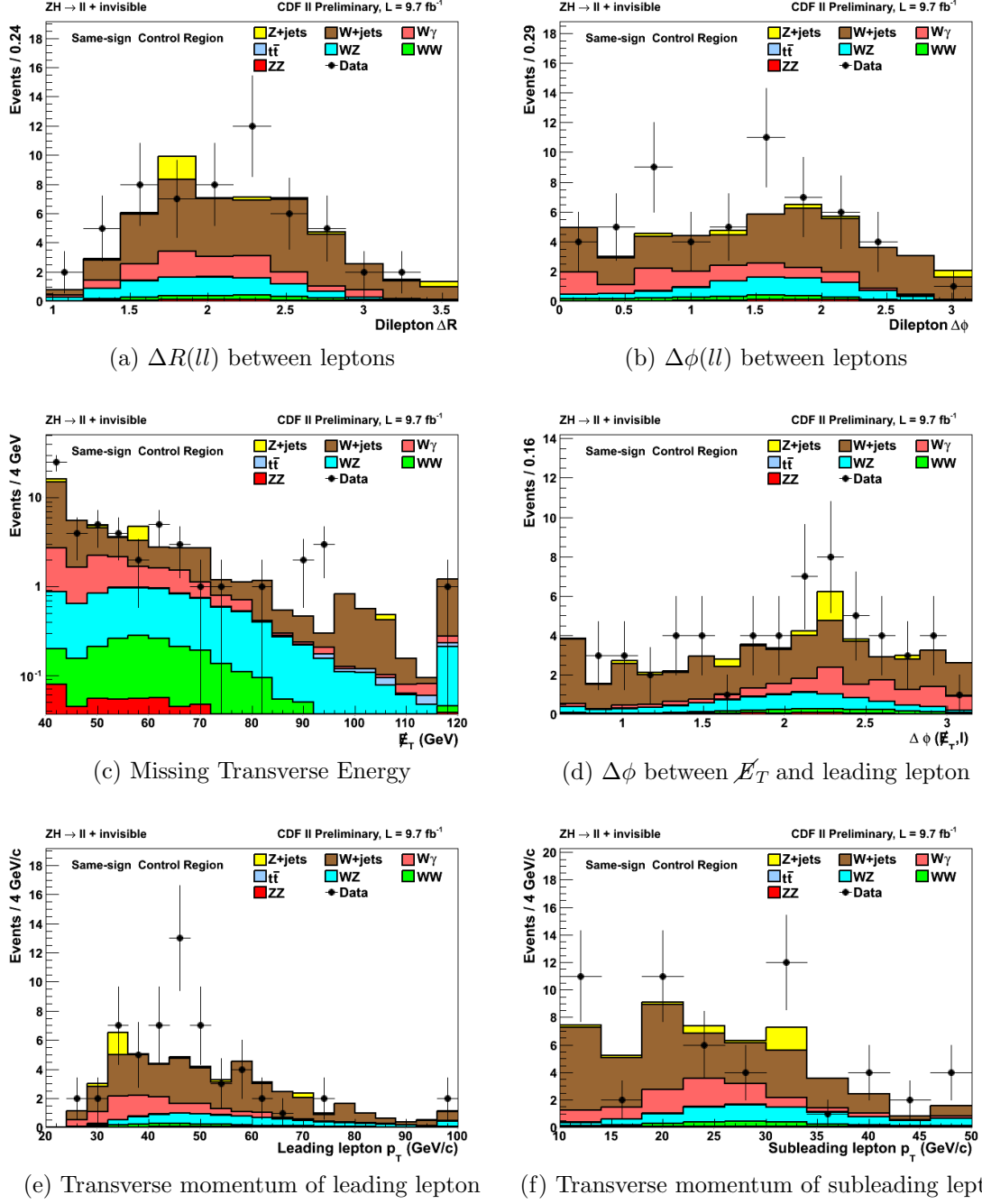
(f) Transverse momentum of subleading lepton

Figure 5.3: Same-sign, same-flavor control region

5.2.3 Side Bands Control Region

To test the WW modeling in a kinematic region similar to the Signal Region we select events with two isolated leptons in the final state satysfing all the requirements that define the Signal Region, but in Side Bands mass range. Selecting two leptons with an invariant mass far from the Z-mass we drastically reduce contribution from real Z. We modify the Signal Region requirements as follow:
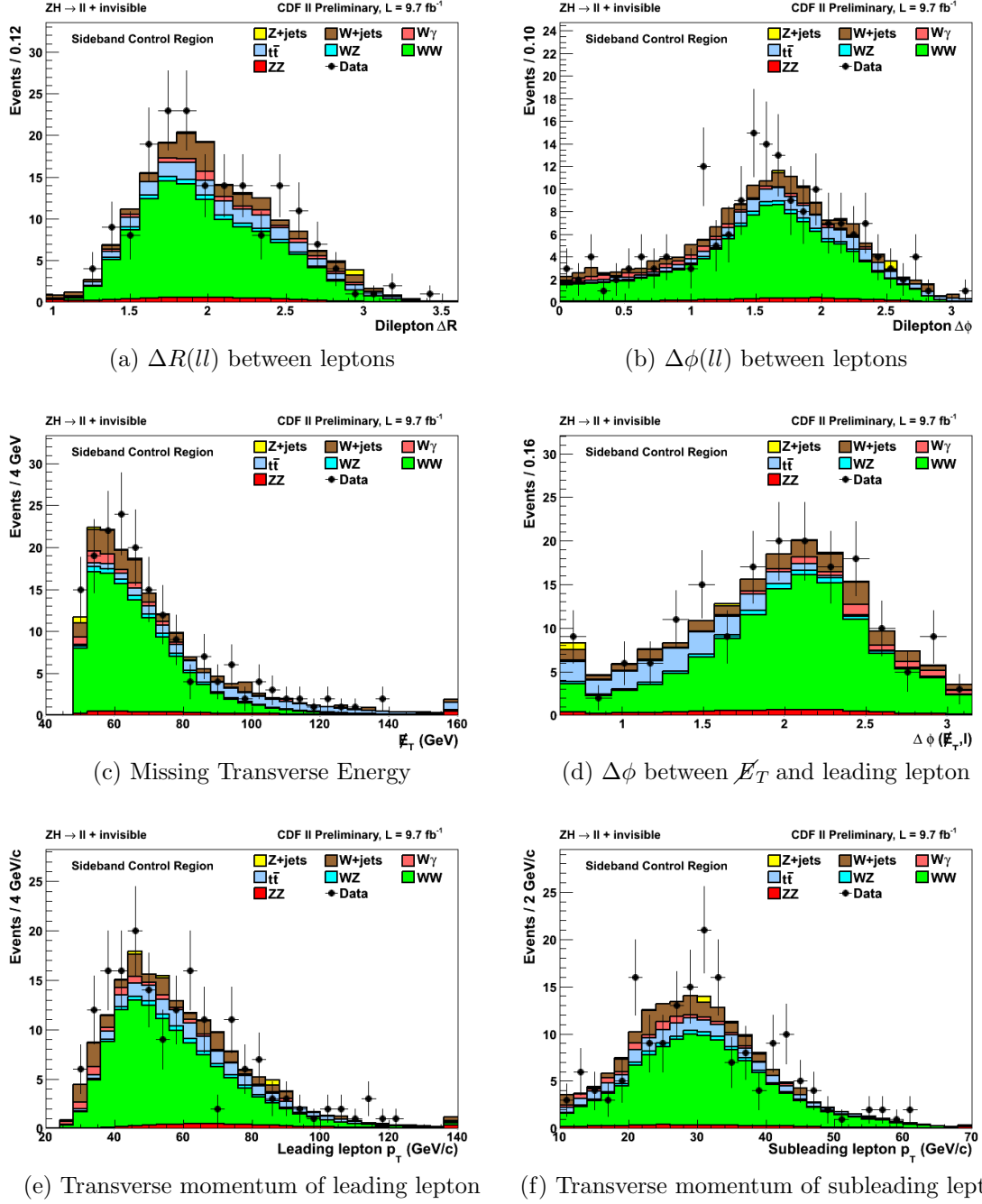
- Different Charge and Same Flavor lepton pair

- $M_{ll} \in [50, 82] \cup [100, 132] GeV/c^2$

- $\not{E}_T \geq 60$ GeV

- No jet with $E_T \geq 15 GeV$ (L5 corrections) with $\Delta\phi(Z, j) \geq 2.0 rad$

- $\min\Delta\phi(\not{E}_T, l) \geq 0.5$ rad

Table [5.4] summarizes the number of events expected from the several processes and the yields in the collected data. The most relevant kinematic variable distributions of the events in the Side Bands Control Region for data and Monte Carlo are shown in Figures [5.4].

No significant discrepancy is noticeable in the data-to-simulation comparison, with uncertainties dominated by the limited statistics of the sample considered. Once tested in this sample, we can assume that the simulation properly models the W+jets background also in the Signal Region.

Table 5.4: Number of predicted and observed events in the Side Bands Control Region, e^+e^-, $\mu^+\mu^-$ pair, no jet with $E_T \geq 15\,GeV$ with $\Delta\phi(Z,J) \geq 2.0$ rad, $M_{ll} \in [50, 82] \cup [100, 132]GeV/c^2$, $\Delta\phi(MET,l) \geq 0.5$ rad, $\not{E}_T \geq 50GeV$

$ZH \rightarrow \ell^+\ell^-$ + invisible (sideband control region)	
CDF Run II Preliminary, $\mathcal{L} = 9.7$ fb^{-1}	
Z +jets	1.7 ± 0.7
$W + jets$	19.8 ± 3.0
$W\gamma$	6.2 ± 1.0
$t\bar{t}$	20.1 ± 3.3
WZ	5.2 ± 0.6
WW	113.4 ± 10.4
ZZ	6.2 ± 0.7
Total prediction	172.7 ± 13.7
Data	177

(a) $\Delta R(ll)$ between leptons

(b) $\Delta\phi(ll)$ between leptons

(c) Missing Transverse Energy

(d) $\Delta\phi$ between $\not{E}_T$ and leading lepton

(e) Transverse momentum of leading lepton

(f) Transverse momentum of subleading lepton

Figure 5.4: Sideband M_{ll} $[50, 82] \cup [100, 132] \mathrm{GeV}/c^2$ control region

Chapter 6

Invisible Higgs search

6.1 Extrapolation to the signal region

A large number of kinematic variables are being considered for their signal-to-background discriminating power, listed below:

- ΔR is the quasi-angular distance value commonly used to measure the distance between two high P_T objects in collider physics, defined as $\Delta R = \sqrt{\Delta\phi^2 + \Delta\eta^2}$, where ϕ is the azimuthal angle around the beamline and η is the pseudorapidity

- $\Delta\phi(\ell\ell)$ is the angular separation between the P_T^1 of lepton 1 and P_T^2 of lepton 2

- $\not{E}_t$ is the missing transverse energy of the signal, being high because of the Higgs boson decaying invisibly

- $\Delta\phi(\not{E}_t, \ell)$ is the magnitude of the difference in asimuthal angle between the most forward lepton by P_T and the $\not{E}_T$.

- P_T^2 is the transverse momentum of the most forward lepton. Separation between signal and background contributions is achieved by requiring the $\not{E}_T$ to be antialigned with the direction of the reconstructed Z boson P_T .

- P_T^1 is the transverse momentum of the most backward lepton. The signals tend to produce pairs of leptons with similar momenta, so the second lepton by P_T trends higher for signals than backgrounds.

We selected as final discriminant the ΔR variable, since the significance of this variable has the highest value between all the kinematic variables we reconstructed, in order to estimate an Upper Limit for the $ZH \to ll\nu\nu$ process.

In the Figure[6.1 the kinematic variable distribution of the events for data
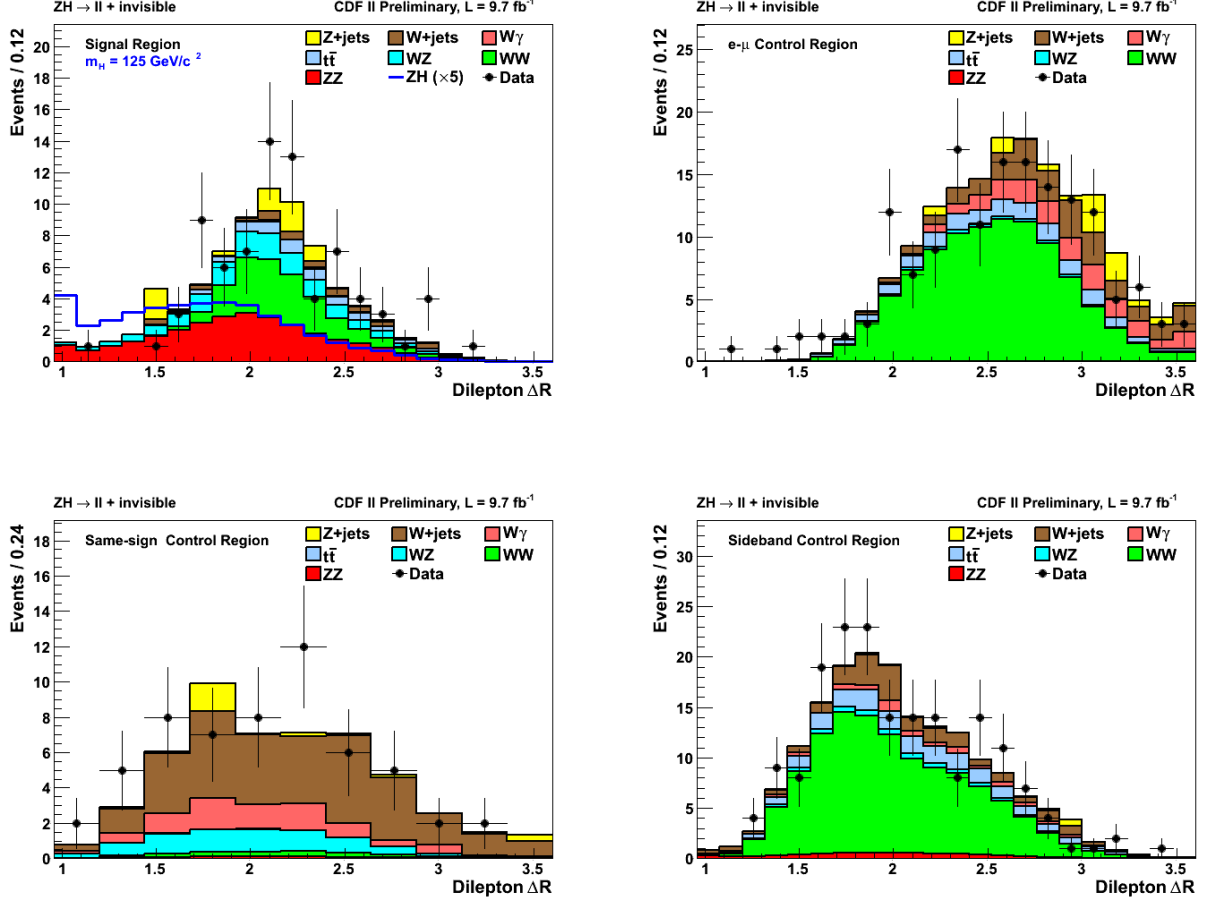and Monte Carlo is shown.

Figure 6.1: Final Discriminant $\Delta R(ll)$

6.2 Statistical interpretation: A Bayesian approach

To exclude a possible signal, or to compute the significance of one that is observed, the measured data must be compared with the predictions of a model which includes new physics, and also a model which does not, to see which of the two (if either) can be excluded, and at what confidence level. In the CL_s limit-setting technique used at LEP [43], the data are compared against two models at a time [44]. One is the null hypothesis, which asserts that the Standard Model describes the data, while the other is the signal+background hypothesis, which asserts that the data are modeled by SM physics plus one or more processes not included in the SM. Uncertainties in the rates and distributions of Standard Model background processes are always present, and can be larger than the predicted signals. If an uncertain prediction is constrained by a subsidiary measurement, for example, by counting events in a control region separated from the signal region, the uncertainties in the modeling are at least partly, and often mostly, statistical in nature.There remain systematic uncertainties in the extrapolation (or interpolation) from a control region to the signal region. Monte Carlo (or data) statistical uncertainties in each bin of a histogram provide an additional source of uncertainty.

The parameters which describe the signal and background processes which are not being measured or constrained by the analysis are called "nuisance parameters". Their values are needed in order to extract measurements of, or limits on, the parameters of interest, and uncertainty in their values usually results in reduced sensitivity to the parameters of interest. The systematic errors on observables are parameterized in terms of these nuisance parameters. To compute discovery or exclusion signficances, the uncertainties in the model predictions must be taken into account; uncertainty in model predictions allows models to be more compatible with any observed data. Choosing which of two models is preferred by the data is made more difficult if the models have degrees of freedom which allow them to accomodate the data by adjusting their nuisance parameters appropriately. Estimations of the sensitivity of an analysis depend crucially on controlling the systematic uncertainties of the model predictions, as well as on collecting large data samples. Typical model uncertainties in histograms of predicted event counts from various processes are rate uncertainties and shape uncertainties. Monte Carlo (or data) statistical uncertainties are present in each bin of a histogram used as part of a model.

A typical analysis on CDF may fit a function to a data histogram, using, for example, mass sidebands and a background fit function to predict the

background underneath a signal peak. Alternatively, events in a separate histogram, collected with different selection requirements, may be used to normalize one or more background contributions in the signal region. Limits are calculated in the CL_s technique by generating pseudoexperiments, randomly varied within the statistical and systematic uncertainties, and comparing the distribution of a test statistic, such as the logarithm of the likelihood ratio, of the data against distributions obtained assuming just the null hypothesis or the hypothesis that new physics is present. It is important to treat each pseudoexperiment in the same way as the data are treated - hence sideband fits or subsidiary experiments must be also simulated and fit, and backgrounds projected into the signal region. A choice of a test statistic which is usually optimal is the likelihood ratio

$$Q = \frac{P(data|H_1)}{P(data|H_0)} \tag{6.1}$$

where H_1 is a model including new physics, and H_0 is the null hypothesis, that new physics is absent. Both H_1 and H_0 predict data counts in each bin of the data histograms to be studied, and these predictions are usually sums from distinct processes, added incoherently. Processes that add coherently should be treated as a single process. For example, in a Z search, $(Z^* \to Z\gamma)$ can be considered just one process if interference is important, while fakes are another process. $P(data|H_1)$ and $P(data|H_0)$ are sensitive to the fact that H_1 and H_0 may be poorly specified. The approach taken here is that used by analysis techniques which find the best-fit model to the data, where these probabilites are maximized over the space of of possible values of the nuisance parameters. The χ^2 function described in CDF 7904 [45] is based on the likelihood function and the test statistic of Equation 6.1 is given by

$$-2\ln Q = \chi^2 P(data|H_1) - \chi^2 P(data|H_0) = \Delta\chi^2 \tag{6.2}$$

The uncertainties which are considered in that chisquared function are rate uncertainties, histogram shape uncertainties, bin-by-bin Poisson statistical uncertainties in the model predictions, and correlations between nuisance parameters.

Asymmetric errors

The χ^2 function of CDF 7904 uses systematic uncertainties on rates that are parameterized by a symmetric, multiplicative scale factor. The rate for a specific process prediction in a particular bin is sensitive to a particular

nuisance parameter

$$r_{ij}^{\text{varied}} = r_{ij}^{\text{central}} \prod_k (1 + s_k f_{kj}) \tag{6.3}$$

where i runs over histogram bins, j indexes which model component is being considered, and k indexes the nuisance parameters s_k which are Gaussian distributed around zero with unit width (except when truncated to keep the model prediction non-negative for all components of the model). The quantity f_{kj} is the fractional uncertainty on the rate of the r_{ij} histogram due to the kth nuisance parameter. Often, one will have two values - one positive and one negative. Rather than generating pseudoexperiments with a discontinuous PDF for a nuisance parameter (like the signal efficiency), it is better to just parameterize the efficiency quadratically on a smoothly varying nuisance parameter. The variation considered here is given by

$$r_{ij}^{\text{varied}} = r_{ij}^{\text{central}} \prod_k (1 + s_k \frac{f_{kj}^+ - f_{kj}^-}{2} + s_k^2 \frac{f_{kj}^+ + f_{kj}^-}{2}) \tag{6.4}$$

The quantity f_{kj}^+ is the fractional change in the rate for process j when the nuisance parameter s_k is positive one unit and f_{kj}^- is the fractional change in the same rate when s_k is negative one unit. For symmetric uncertainties, $f_{kj}^+ = -f_{kj}^-$.

Histogram interpolation and extrapolation

Histograms are interpolated within their shape uncertainties on each pseudo-experiment. Histograms may be interpolated "horizontally" or "vertically". Vertical interpolation is just a linear interpolation of bin contents, with the restriction that bin contents cannot be negative. Horizontal interpolation is more appropriate when the shape variations shift the values of the variables being histogrammed. An example is the above jet energy scale uncertainty shifting m_{jj} up and down. Vertical interpolation may be more appropriate for neural net output histograms, where horizontal interpolation may produce spurious third peaks when interpolating two histograms each with peaks at 0 and 1 and nothing in between. In general, histogram interpolation is a much more reliable procedure than histogram extrapolation, and so the ROOT package MINUIT minimization procedure used to minimize the χ^2 test statistic is not allowed to sail into a portion of nuisance parameter space which requires histogram extrapolation. It is therefore up to the user of the software to provide shape variations of several sigma. Providing $\pm 1\sigma$ shape variations will truncate the considered space of nuisance parameter values to

$\pm\sigma$.

Fortunately, a routine is provided which can also extrapolate histograms in the cases for which shape variations are available but only for relatively small excursions of the nuisance parameters. Compounded interpolation is necessary since a model varying more than one nuisance parameter at a time may be needed to fit the data properly. For example, fitting a Gaussian requires varying both the mean and width simultaneously, and the nonparametric interpolations supplied with this program allow fitting more general sets of parameters. Furthermore, if two nuisance parameters both shift a template histogram by the same amount in the same way, constructing a model in which both nuisance parameters take on the value $+1\sigma$ should involve shifting the template twice as much in that way. In this manner, compounding several nuisance parameters' shape variations amounts to an extrapolation. With vertical interpolation, the variations from the central histogram due to interpolation in each of the nuisance parameters are added linearly, and no bin is allowed to go below zero. With horizontal interpolation, the horizontal variations in the cumulative histograms are added linearly, and the cumulative histogram is not allowed to "bend", which could happen if two shape variations sharpened up a peak. While neither one is allowed to go beyond its maximum range in the program, varying both simultaneously could result in sharpening up a peak beyond a delta function. This is protected against in the code by insisting that the cumulative histogram be monotonically increasing.

Confidence level calculation

The Gaussian χ^2 distribution, computed by routines such as CERNLIB's PROB function, do not apply in the more general case considered here, since the variations of each measaurement are Poisson and not Gaussian. To interpret the χ^2 values, pseudoexperiments must be generated and the observed χ^2 values must be compared against distributions obtained in different hypotheses. The confidence level for excluding H_1, given some experimental data and a null hypothesis, is given by the probability that Q is less than that obtained in the data, Q_{obs}, assuming the new-physics hypothesis H_1

$$CL_{H_1} = P_{H_1}(Q \leq Q_{obs}) = P_{H_1}(\Delta\chi^2 \geq \Delta\chi^2_{obs}) \tag{6.5}$$

$$\tag{6.6}$$

This hypothesis is excluded at the 95% CL if $CL_{H_1} = 0.05$, and at more than the 95% CL if $CL_{H_1} < 0.05$. The confidence level for excluding the

background is given by

$$1 - CL_{H_0} = P_{H_0}(Q \geq Q_{obs}) = P_{H_0}(\Delta\chi^2 \leq \Delta\chi^2_{obs}) \tag{6.7}$$

This is the probability that the null hypothesis will give an outcome that looks at least as signal-like as the one observed. For discovery, $1 - CL_{H_0}$ is required to be no more than 2.87×10^-7 , or twice that, depending on how one interprets what is meant by "five sigma", including just one side of a Gaussian tail or both. The quantity

$$CL_s = \frac{P_{H_1}(\Delta\chi^2 \geq \Delta\chi^2_{obs})}{P_{H_0}(\Delta\chi^2 \geq \Delta\chi^2_{obs})} \tag{6.8}$$

is better behaved for exclusion than CL_{H1} alone because it cannot be used to exclude a hypothesis to which there is no experimental sensitivity, while in the case of CL_{H_1} , 5% of those hypotheses for which there is no sensitivity will be excluded at the 95% CL. The confidence level for excluding the signal + background is

$$CL_{s+b} = P_{s+b}(Q \leq Q_{obs}) = P_{s+b}(\Delta\chi^2 \geq \Delta\chi^2_{obs}) \tag{6.9}$$

The numerator and the denominator denominator of CLs must also include the probability of the observed outcome, and so the definitions above with the appropriate inequalities are a precise statement of what needs to be done. The difference between using $\leq$ and $<$ becomes large for experiments with a small number of expected events and only one bin in the histogram. Splitting the data up into many bins with different signal-to-noise ratio expecations reduces the probability of any single outcome and also makes the analysis more optimal. These probabilities, $P_{H_0}(Q \geq Q_{obs})$ and $P_{H_1}(Q \leq Q_{obs})$ need to be computed assuming a sample space from which the observed experiment is drawn, commonly called an "ensemble". To compute these probablilites, pseudoexperiments are drawn from this ensemble, and the pseudodata are analyzed in the same way as the real data, to compute $\Delta\chi^2$ for each possible outcome. If the hypotheses H_1 and H_0 were perfectly specified, this would consist of generating Poisson random numbers in each bin of each histogram according to the perfect predictions. For this analysis probabilities are computed as

$$P_{s+b}(Q \leq Q_{obs}) = \sum_{Q(d_i) \leq Q(d'_i)} \prod_i^n e^{-(s_i+b_i)} \frac{(s_i + b_i)^{d'_i}}{d'_i} \tag{6.10}$$

where $Q(d_i)$ is computed for the observed candidates for each channel d_i and the sum is over final outcomes d'_i with test statistic value less than or equal

to the observed one. For the purposes of this analysis, the likelihood ratio is chosen to be the test statistics Q, as the the ratio of the likelihood function for the background-plus-signal hypothesis to the likelihood function for the background-only hypothesis.

$$Q = \prod_i^n \frac{e^{-(s_i+b_i)} \frac{(s_i+b_i)^{d'_i}}{d'_i}}{e^{-(b_i)} \frac{(b_i)^{d_i}}{d_i}} \qquad (6.11)$$

where s_i is the signal expectation in the i-th bin of he discriminating variable, b_i is the background expectation, and d_i is the number of events observed in data.

The problem is that systematic uncertainties in the models prevents precise interpretation of a specific outcome of the data since it is not known from what sample space it was drawn. A Bayesian approach to this problem is to integrate the probability of each outcome over the values of all of the nuisance parameters, weighted by the prior belief functions for each nuisance parameter (typically Gaussians, or truncated Gaussians to keep predictions from being negative). This procedure is called "marginalization and is in common use in Bayesian techniques and mixed Bayesian-Frequentist techniques. To include the systematic errors, let Q_i be the ith term in the product of expression 6.11. Then replace the errorless test statistic Q'_i with Q_i

$$Q'_i = \frac{\int_0^\infty ds' \int_0^\infty db' e^{\frac{-(\frac{(s'-s_i)^2}{2\sigma_s^2} + \frac{(b'-b_i)^2}{2\sigma_b^2})}{2\pi\sigma_s\sigma_b}} Q_i}{\int_0^\infty ds' \int_0^\infty db' e^{\frac{-(\frac{(s'-s_i)^2}{2\sigma_s^2} + \frac{(b'-b_i)^2}{2\sigma_b^2})}{2\pi\sigma_s\sigma_b}}} \qquad (6.12)$$

An exclusion of at least 95% confidence level is achieved if $CL_{s+b} \leq 0.05$. The confidence level reported by this analysis will be normalized to the Standard Model background hypothesis $CL/\sigma_{ZH \times \mathcal{B}(H \to \text{invisible})}$. Hence, $CL/\sigma_{ZH \times \mathcal{B}(H \to \text{invisible})} = 1$ means that the background-plus-signal hypothesis has been excluded at 95% confidence level. This is then compared to the same confidence level normalized to invisibly decaying Higgs boson computed with pseudoexperiments assuming the background hypothesis and normalized to the amount of data available to date. When an insufficient amount of data has been collected to distinguish the $s+b$ hypothesis from the b hypothesis, $CL/\sigma_{ZH \times \mathcal{B}(H \to \text{invisible})} > 1$. As more data is collected, this value decreases. When these pseudoexperiments assuming the background hypothesis achieve $CL/\sigma_{ZH \times \mathcal{B}(H \to \text{invisible})=1}$, we say we have "achieved invisible Higgs boson sensitivity" at the 95% confidence level.

Marginalization is necessary in order to incorporate the effects of systematic uncertainty in the confidence limits. Without marginalization of the probabilities of each outcome, systematic uncertainties would be ignored entirely in this case. The goal is to treat all the statistical uncertainties in a frequentist manner, by generating Poisson random numbers or event-counting processes in the main and subsidiary experiments, and by marginalizing over the remaining nuisance parameters. No general assumption is made on the distribution of $\Delta\chi^2$ in either hypothesis, instead it must be computed from the scratch for each model tested. Optimizing for exclusion usually involves improving signal acceptance at the cost of letting in more background. Separating events into high signal-to-background ratios and low signal-to-background ratios classes and combining the results gives optimal sensitivity for all cases. When excluding new physics models, 95% CL exclusion is usually the criterion chosen, and one only has to compute CLs with enough precision to tell that an observed outcome is less probable than about 5% of the time assuming a signal is present. But forming discovery p-values, we must compute $1 - CL_{H_0}$ values of the order of 1×10^{-7} . This computation involves generating of the order of 1×10^8 pseudoexperiments, just to be on the safe side. The traditional solution is to compute the probability in the tail of a χ^2 distribution if one knows the number of degrees of freedom, using the CERNLIB PROB function. One problem here is that the distribution of the $-2lnQ$ test statistic is not a true chisquared distribution due to the Poisson nature of the data. If the signal-to-background ratio of all bins of the analysis is very small , one can approximate the distributions as Gaussian and do away with needing to run psuedoexpeirments (although enough should be run to verify the shape of the core of the distribution).

An issue comes up when the search analysis has a mixture of one or more channels or bins with a low expected signal-to-background ratio and a large expected event rate, which are combined with one or more bins with low backgrounds and higher signal-to-background ratio. The PDF of the test statistic is then a convolution of a Gaussian chisquare distribution with a discrete Poisson distribution. The inclusion of the fit to maximize the likelihood for each hypothesis further distorts the picture. It is hard to make a prediction of the form of the PDF of the test statistic without doing pseudoexperiments.

Software

A limit calculator is based on the $\Delta\chi^2$ test statistic described above, and the program runs as a compiled script in ROOT. The inputs are 1D and 2D histograms. It is built on the $\Delta\xi^2$ calculator described in CDF 7904, which has

been extended to compute a joint chisquare over many histograms of data, so that several searches for new physics may be combined together. The code is available at *http://www.hep.uiuc.edu/ home/ trj/ cdfstats/ mclimit_csm1/ index.html*, along with some examples of how to use it. One uses this package by creating a member of the ROOT class *mclimit csm* and creating instances of the class *csm model* which describe the signal and null hypotheses. Instances of class *csm model* have inside of them template histograms which are fit to the data, as well as descriptions of all of the systematic uncertainties and their correlations. Separate instances of csm model are used to generate pseudoexperiments and to fit them, so that the user may study the effects of estimated central values used in the fits for backgrounds, for example, which are systematically different from the ones used to generate pseudoexperiments. No statistical technique can protect against incorrectly estimated backgrounds with underestimated systematic uncertainties, but at least the tools to minimize the impact and to study the residual effects are provided.

A channel corresponds to one data histogram, and typically corresponds to a single analysis team's result. Subsidiary experiments should be included as separate channels, although mass sidebands that are included in the same histogram and fit together are included in the same channel as the signal. A channel model, of class *csm channel model*, consists of template histograms for the components to sum up to predict the event counts in each bin, as well as uncertainties in rates and shapes. A *csm model* is a collection of *csm channel model*'s, along with optional constraint relationships between nuisance parameters.

Most correlations in systematic uncertainties are handled simply by using the same nuisance parameter name to refer to effects on two different distributions. For example, if the jet energy scale affects the signal acceptance and the background rate and their shapes, then the nuisance parameter named after the jet energy scale should be re-used to parameterize all of those uncertainties, so that they move together in the pseudoexperiments and in the fits. Nuisance parameters with the same name are taken to be 100% correlated and nuisance parameters with different names are taken to be 0% correlated (unless an equation of constraint is supplied). Arbitrarily-correlated systematic errors can always be decomposed into 100% and 0% correlated pieces.

The data histograms are supplied, identified by their channel names. The members of class *csm model* refer all template histograms to the channel to which they correspond. The Bayesian ensemble is generated using the test-hypothesis pseudoexperiment model, since it is the one which is expected to list all the signals and backgrounds with all of their correlated errors. The test-hypothesis model, used to fit to the pseudodata, may in many situa-

tions, be a stripped-down model with fewer nuisance parameters to fit than are varied. The expected limits are computed by generating null-hypothesis pseudoexperiments (using the null-hypothesis pseudoexperiment model) and then interpreting them just like the data.

6.3 Systematic uncertainities

The systematic uncertainties considered in this measurement affect both predicted signal and background contributions to all the discriminating variable distributions for each of the contributing processes. The systematics uncertainties considered in this analysis are summarized in Table 6.1 and are:

- **Lepton ID Efficiency:** Systematic uncertainties due to the lepton ID efficiencies are calculated by coherently varying the lepton ID scale factors by 1σ for each lepton and counting the number of expected events. From a signal MC sample a variation of $\pm 3.6\%$ is found.

- **Trigger Efficiency:** The trigger efficiencies are varied up and down by their 1σ uncertainties to determine the % change in the acceptance, which is taken to be the systematic error. The trigger efficiencies are varied in a correlated way. The variation is found to be $\pm 2.1\%$.

- **Luminosity:** A systematic of $\pm 6\%$ is used on the total luminosity, as suggested from the Joint Physics group.

- **Cross Section:** The cross-section has been computed at NNLO+NNLL precision with the associated scale and PDF variations following the PDF4LHC prescription (see .2).

- **NLO effects on the acceptance on ZZ production:** The Pythia ZZ production Monte Carlo used for acceptances and efficiencies determination is at LO. Using MCFM [46] the difference in the acceptance due to a full NLO simulation is found to be $\pm 2.5\%$, which is assigned as a systematic uncertainty.

- **MC $\not{E}_T$ modelling uncertainty:** The uncertainty in fake $\not{E}_T$ following studies of the Drell-Yan background in $H \rightarrow WW$ searches is assigned.

- **Fake rates uncertainties:** Fake probabilities, or the probability that a jet-like object will be falsely identified as a lepton, are calculated using the jet-triggered data samples. These fake probabilities are calculated

as a function of both lepton type and $\not{E}_T$ (or P_T). These probabiities are then applied to the W+jets (fakeable object) sample from data. The fake probabilities are varied up and down to get an estimate of the uncertainty on the yield. This systematic only applies to the fakes (or W+jets) sample.

$ZH \to \ell^+\ell^-$ + invisible				CDF Run II Preliminary, $\mathcal{L} = 9.7$ fb^{-1}				
Systematic Uncertainties (%)	ZZ	WZ	WW	$t\bar{t}$	$W + jets$	$Z + jets$	$W\gamma$	ZH
Theory cross section	6	6	6	10		33	10	5
NLO acceptance	5	5		10			5	10
Luminosity	5.9	5.9	5.9	5.9			5.9	5.9
Electron conversion							10	5.9
Jet-energy scale	2	4	1	4		28	3	1
Initial/final state radiation								8
Fake lepton rate					15			
Lepton ID	3	3	3	3		3		3
Trigger efficiency	2	2	2	2		2		2

Table 6.1: Table of the Systematic uncertainties considered in the measurement

To extract the $\sigma(ZH) \times \mathcal{B}(H \to inv.)$ production cross section, a Bayesian method is employed (see section 6.2), building a likelihood function that takes as inputs the expected signal acceptance, the number of expected background events, and the number of observed events passing the selection criteria described above. The resulting expression gives the Poisson probability for obtaining the observed number of events as a function of the $\sigma(ZH \to \ell\bar{\ell}\, inv.)$ value, to which we assign a uniform prior probability over the range of non-negative values. The function also includes terms for truncated, Gaussian-constrained nuisance parameters corresponding to each systematic uncertainty source, which are integrated over their parameter space.

6.4 Results

In Figs. 6.2, 6.3 the 95% CL limits for the exclusion of $H \to inv.$ process are shown, for the assumed prediction for σ_{ZH} and with no assumptions on it, respectively. The expected limit line (black dotted line) going over the value 1.0 indicates Higgs boson masses at which CDF is now sensitive for excluding the existance of a invisibly decaying Higgs boson at 95% CL, assuming it does not exist. The observed line (solid line) indicates the Higgs boson masses at which CDF has indeed experimentally excluded the existence of the invisibly decaying Higgs boson at 95% CL. If the non-SM Higgs boson did exist at

these masses, the one would expect to see the observed line recording a much lower value than the expected line. The observed line heading outside of the yellow bands indicates a 2 standard deviation signal. If the observed line were 3 standard deviations below the expected line (out of the yellow bands), then one would have "evidence" of a signal. If the observed line were 5 standard deviations below the expected line, then one would have "discovered" a signal. A blue dotted line corresponds to the expectation for the inclusion of the invisibly decaying SM Higgs boson. Therefore,
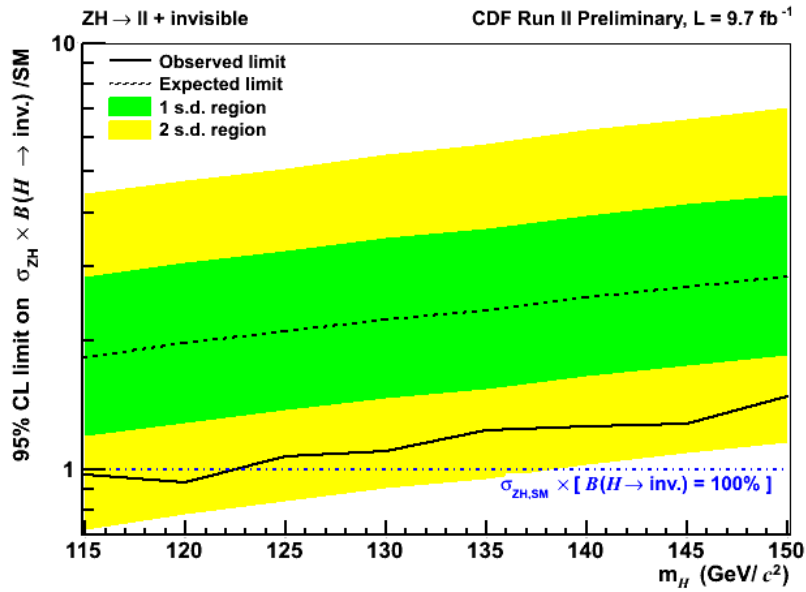

Figure 6.2: 95% credibility limits for Higgs boson production normalized to the assumed prediction for $\sigma_{ZH} \times \mathcal{B}(H \rightarrow inv.)$. The branching ratio is assumed to be 100%, whereas the production cross section is assumed to be the SM prediction for ZH production.

in $L = 9.7$ fb^{-1} of data analyzed there is no evidence for a Higgs boson decaying invisible in the mass range considered so a 95% CL upper limit on the Higgs decaying cross section can be set. The exact points of the 95% credibility upper limits for Higgs boson decays are given in the table 6.2. A combination of matrix element and neural network techniques could be used to discriminate signal from background for all the existent control variables, but in this analysis only one discriminating variable, semi-angular separation between the leptons ΔR has been used.
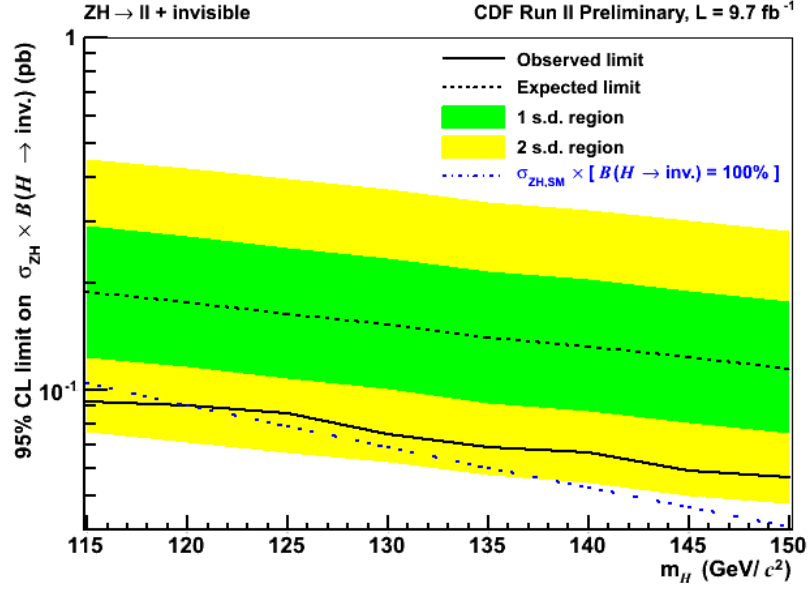
Figure 6.3: 95% credibility limits for $\sigma_{ZH} \times \mathcal{B}(H \rightarrow inv.)$. No assumption on the cross section or branching ratio is made for the expected and observed results.

$ZH \rightarrow \ell^+\ell^-$ + invisible	CDF Run II Preliminary, $\mathcal{L} = 9.7$ fb^{-1}					
m_H (GeV/c^2)	95% C.L. on $\sigma_{ZH} \times \mathcal{B}(H \rightarrow \text{invisible})/\sigma_{ZH,\text{SM}}$					
	-2 s.d.	-1 s.d.	**Exp.**	+1 s.d.	+2 s.d.	**Obs.**
115	0.73	1.19	**1.82**	2.81	4.37	**0.93**
120	0.79	1.29	**1.97**	3.04	4.78	**0.97**
125	0.84	1.37	**2.10**	3.26	5.08	**1.04**
130	0.90	1.46	**2.23**	3.47	5.47	**1.16**
135	0.95	1.53	**2.35**	3.64	5.77	**1.17**
140	1.03	1.65	**2.52**	3.91	6.18	**1.26**
145	1.09	1.75	**2.67**	4.16	6.64	**1.38**
150	1.15	1.85	**2.82**	4.38	6.97	**1.37**

Table 6.2: Upper Limits for each mass between $115 \leq m_H \leq 150$ GeV/c^2

Chapter 7

Conclusions

The Standard Model of particle physics is extraordinarily successful at describing our observations, but it does not provide a complete picture of our universe. It does not, for example, provide a dark matter candidate or an explanation for why the masses of fundamental particles such as electron and muon are so different. The recently confirmed existence of a Higgs-like boson provides a new opportunity to test the consistency of the SM with our observations and search for physics Beyond the Standard Model (BSM).

Weak experimental constraints on the Higgs decay width caused by limitations in detector resolution leave room for BSM decays. The Higgs decay width to invisible particles is an especially interesting property to be measurable with the existing detectors. This width has a small value in the Standard Model, but BSM effects can make it large enough to measure.

In this thesis, we present the first search at the Tevatron for a Higgs boson decaying to an invisible final state. The search is performed in $\sqrt{s} = 1.96$ TeV proton-antiproton collision events collected with the CDF detector. The full CDF Run II data sample, corresponding to an integrated luminosity of 9.7 fb^{-1}, is used.

We search in the associated ZH production mode. Decays of the Z boson to electron and muon pairs provide the cleanest signatures for detection at hadron collider experiments because they can be identified in a trigger and have a small background. Events are required to have two same-flavor, oppositely charged electrons or muons and a significant value of missing transverse energy. Control samples in the data are used to measure the background. The control samples are constructed from events with low missing transverse energy or pairs of leptons with opposite flavor, identical charge, or with an invariant mass outside the Z mass window.

Selected events are binned in $\Delta R(\ell\ell)$ between the two leptons in the pseudorapidity-azimuthal angle space. Following the Bayesian approach, a binned likelihood

function is constructed from a product of likelihoods for obtaining the results observed in each bin based on expected signal acceptance, the number of expected background events, and the number of observed events. No excess above SM predictions is found. Therefore, 95% CL upper limits on the Higgs invisible decay are placed for a a Higgs-like boson in the 115 to 150 GeV/c^2 mass range. The analysis excludes cross section values of $H \rightarrow$ invisible, produced in association with $Z \rightarrow \ell^+\ell^-$, larger than 90 fb at a Higgs boson mass of 125 GeV/c^2 .

My most important contributions to the analysis included estimating selection efficiencies, developing a new Z+jets background estimate to address Monte Carlo mis-modeling, optimizing the discriminating variable used in statistical tests, and computing upper limits. I presented the analysis in the CDF Top/BSM group, and obtained its approval. Following the approval, I presented this work at Les Rencontres de Physique de la VallÃ©e d'Aoste, La Thuille 2014, and ICHEP 2014, Valencia. I am currently working on incorporating dark matter signal models. After including these additional interpretations, this work will be submitted for publication.

Appendices

.1 Background modeling

The acceptances for the $H \to WW$, WW, WZ, ZZ, $W\gamma$, Drell-Yan, and tt processes are determined using simulated data. Events are simulated with the mc@nlo program for WW [?], PYTHIA for Drell-Yan, WZ, ZZ, and tt [?], and the generator described in Ref. [?] for $W\gamma$. Simulated diboson and tt event samples are normalized to the highest-order theoretical cross section available [?]. The response of the CDF II detector is then estimated with a geant-4-based simulation [?] to which an efficiency correction of up to 10% per lepton is applied based on measurements of the lepton reconstruction and identification efficiencies using observed $Z \to l^+l^-$ events. A correction to fake rate is applied for the small real lepton contribution using Monte Carlo simulation of single W and Z boson production [?].

.2 Parton distribution functions and PDF4LHC prescription

Parton distribution functions (PDFs) describe the structure of colliding hadrons in terms of quarks and gluons. They are vital for the implementation of the MC techniques in this analysis and pose a significant source of systematic uncertainty. The interpretation of existing experimental data in terms of the Standard Model (SM), the precision measurements of SM parameters, as well as the direct search for signals for physics beyond the SM, all rely heavily on calculations based on Quantum Chromodynamics (QCD) and the QCD-parton picture, with the parton distribution (and fragmentation) functions as essential input. The (non-perturbative) parton distribution functions at some given momentum scale are currently determined phenomenologically by a global analysis of a wide range of available hard scattering processes involving initial-state hadrons, using the perturbative QCD-parton framework. At NLO, the recommendation is, for the case described above, to use predictions from the PDF fits from CTEQ, MSTW and NNPDF. These sets all use results from hadron collider experiments, i.e. the Tevatron, as well as fixed target experiments and HERA, and they make available specific sets for a variety of $\alpha_s(m_Z)$ values. The PDFs from these three groups to be used are: CTEQ6.6 [?], MSTW2008 [?] and NNPDF2.0 [?]. In this analysis, CTEQ parametrisation is used. For the calculation of uncertainties, it is prescribed to use the envelope provided by the central values and PDF$+\alpha_s$ errors from the MSTW08, CTEQ6.6 and NNPDF2.0 PDFs, using each group's prescriptions for combining the two types of errors. The usage of this type of envelope is justified because the deviations between the

predictions are as large as their uncertainties. As a central value, the midpoint of this envelope is recommended. A 68% CL uncertainty envelope is to be calculated and consistently the 68% CL α_s variations. Note that the CTEQ6.6 set has uncertainties and α_s variations provided only at 90% CL and thus their uncertainties should be reduced by a factor of 1.645 for 68% CL. Within the quadratic approximation, this procedure is completely correct. At NNLO, the calculation is to be based on PDF uncertainties on the only NNLO set which currently includes a wide variety of hadron collider data sets, i.e. MSTW2008 [**?**]. There seems to be no reason to believe that the spread in predictions of the global fits, i.e. MSTW, CTEQ and NNPDF, will diminish significantly at NNLO compared to NLO, where this spread was somewhat bigger than the uncertainty from each single group. Hence, at NNLO the uncertainty obtained from MSTW alone should be expanded to some degree. It seems most appropriate to do this by multiplying the MSTW uncertainty at NNLO by the factor obtained by dividing the full uncertainty obtained from the envelope of MSTW, CTEQ and NNPDF results at NLO by the MSTW uncertainty at NLO. In all cases the α_s uncertainty should be included. We note that in most cases so far examined for the LHC running at 7 TeV center-of-mass energy this factor of the envelope divided by the MSTW uncertainty is quite close to 2, and this factor can be used as a short-hand prescription.

Bibliography

[1] ATLAS Collaboration, *CERN-PH-EP-2012-218*, arXiv:1207.7214 (2012)

[2] CMS Collaboration, *CMS-HIG-12-036, CERN-PH-EP-2013-035* arxiv:1303.4571, (2013)

[3] CDF and D0 Collaborations and the Tevatron New Physics and Higgs Working Group, *FERMILAB-CONF-12-318-E, CDF-NOTE-10884, D0-NOTE-6348*, arxiv:1207.0449, (2012)

[4] I. J. R. Aitchison and A. J. G. Hey. *Gauge Theories in Particle Physics: A Practical Introduction.* Adam Hilger, 1989.

[5] Ahmad et al. Direct evidence for neutrino flavor transformation from neutral-current interactions in the Sudbury neutrino observatory. *Phys. Rev. Lett.*, 89, 2002.

[6] Y. et al. Fukuda. Evidence for oscillation of atmospheric neutrinos. *Phys. Rev. Lett.*, 81, 1998.

[7] K. Nakamura et al. Review of particle physics. *J. Phys.*, G37, 2010.

[8] G. Shaw F. Mandl. *Quantum field Theory.* John Wiley and Sons, 1984.

[9] E. Fermi. *Nuovo Cim.*, 1 (11), 1934.

[10] S. L. Glashow. Partial Symmetries of Weak Interactions. *Nucl. Phys.*, 22:579–588, 1961.

[11] P.W. Higgs. Broken symmetries, massless particles and gauge fields. *Physics Letters*, 12(2), 1964.

[12] F. Englert and R. Brout. Broken symmetry and the mass of gauge vector mesons. *Phys. Rev. Lett.*, 13:321–323, Aug 1964.

[13] G. S. Guralnik, C. R. Hagen, and T. W. B. Kibble. Global conservation laws and massless particles. *Phys. Rev. Lett.*, 13:585–587, Nov 1964.

[14] S. Weinberg. A model of leptons. *Phys. Rev. Lett.*, 19:1264–1266, 1967.

[15] A. Salam. *Elementary Particle Theory.* Almqvist and Wiksells, Stockholm, 1968.

[16] ATLAS Collaboration, *CERN-OPEN-2008-020*, arXiv:0901.0512v3, (2008)

[17] K. Jakobs, *Eur. Phys. J. C* **59** 463-495, (2009)

[18] R. M. Godbole, M. Guchait, K. Mazumdar, S. Moretti and D. P. Roy, *Phys. Lett. B* **571** 184, (2003)

[19] Kiel Howe, Prashant Saraswat, *JHEP 1210 (2012) 065*, arXiv:1208.1542 (2012)

[20] N. G. Deshpande, Dilip Kumar Ghosh, *Phys.Lett. B567* , arXiv:hep-ph/0303160 (2003)

[21] N. Arkani-Hamed, S. Dimopoulos, G. Dvali, J. March-Russell, *Physical Review D* **65** (2) 024032, Arxiv:9811448, (2002)

[22] Y. Chikashige, R.N. Mohapatra, R.D. Peccei, *Phys. Lett. B* **98**, 265, (1981).

[23] Anjan S. Joshipura and Saurabh D. Rindani, *Phys. Rev. Lett. 69, 3269* (1992)

[24] G. Belanger et al, *Phys.Lett. B* **723** 340-347 Arxiv:1302.5694, (2013)

[25] LEP Higgs boson working group, *LHWG Note 2001-06, ALEPH 2001-36 CONF 2001-056, DELPHI 2001-116 CONF 540, L3 note 2702, OPAL Technical Note TN694*, Arxiv:0107032, (2011)
DELPHI Collaboration, *Eur. Phys. J. C* **32** 475, (2004)

[26] Stephen P. Martin and James. D. Wells, *Phys.Rev. D* **60** 035006, Arxiv:9903259v1, (1999)

[27] Shou-hua Zhu, *Eur.Phys.J*, arXiv:hep-ph/0512055, (2006)

[28] A.L. Read, *J. Phys. G* **28**, 2693 (2002)

[29] G. Aad et al. *Phys. Rev. Lett.* **112**, 201802 (2014)

[30] CDF Collaboration, *FERMILAB-Pub-96/390-E*

[31] D. Acosta et al. (CDF Collaboration), *Phys. Rev. D* **71**, 032001, (2005).

[32] J. M. Nett *The search for $VH \rightarrow VWW$ standard model higgs production in the trilepton signature with 5.9 fb^{-1} of data from $p\bar{p}$ collisions at $\sqrt{s} = 1.96$ GeV. Dissertation at University of Wisconsin-Madison*, (2010)

[33] F. Abe et alt. (CDF Collaboration) *The Topology of Three Jet Events in $p\bar{p}$ Collisions at $\sqrt{s}$ = 1.8 TeV* Phys. Rev. D 45 (1992) 1448.

[34] H. Davoudiasl, T. Han and H.E. Logan, *Phys. Rev. D* **71** 115007, Arxiv:0412269, (2005)

[35] D. Cavalli and G. Negri, *ATLAS note, ATLAS-PHYS-2003-009*
J. Thomas, *ATLAS note, ATL-PHYS-2003-003*
R. Kinnunen and A. Nikitenko, *CMS NOTE 2003-006*

[36] B.P. Kersevan, M. Malawski and E. Richter-Was, *Eur. Phys. J. C* **29** 541, (2003)

[37] F. Abe et al. (CDF Collaboration), *Phys. Rev. D* **45**, 001448, (1992)

[38] A. Bhatti et al. (CDF Collaboration), *Nucl. Instrum. Methods A* **566** 375, (2006)

[39] M. Bauce, D. Lucchesi, with the support of the HWW group, Internal note for the 9.7/fb ZZ cross section measurement in the 4l and llvv decay channel (2012)

[40] Peter. W. Higgs, *Phys. Rev. Lett.* **13** 16-17, (1964)

[41] V. Buescher and K. Jakobs, *Int. J. Mod. Phys. A* **20** 2523-2602, (2005)

[42] Marumi M. Kado and Christopher G. Tully, *Annu. Rev. Nucl. Part. Sci.* **52** 65-113, (2002)

[43] S. Baker and R. D. Cousins, *Nucl. Instrum. Meth. A* **221** 437, (1984).

[44] L. Lyons, *OUNP-99-12*, (1999).

[45] T. Junk, *CDF7904*, (2005).

[46] Kyle J. Knoepfel, *CDF/PUB/ELECTROWEAK/PUBLIC/10860*

Acknowledgments